Economic Geology, v. 114, no. 4, pp. 719–744

Zircon Alteration as a Proxy for Rare Earth Element Mineralization Processes in Carbonatite-Nordmarkite Complexes of the Mianning-Dechang Rare Earth Element Belt, China

Yan Liu,[1,2,†] Zengqian Hou,[1] Rongqing Zhang,[2] Ping Wang,[3] Jianfeng Gao,[4] and Markus B. Raschke[5]

[1]*Key Laboratory of Deep-Earth Dynamics of Ministry of Natural Resources, Institute of Geology, Chinese Academy of Geological Science, Beijing 100037, China*

[2]*State Key Laboratory for Mineral Deposits Research, School of Earth Sciences and Engineering, Nanjing University, Xianlin University Town, Nanjing 210023, China*

[3]*School of Physical Science and Technology, Sichuan University, Chengdu, Sichuan 610064, China*

[4]*State Key Laboratory of Ore Deposit Geochemistry, Institute of Geochemistry, Chinese Academy of Sciences, Guiyang 550081, China*

[5]*Department of Physics, Department of Chemistry, and JILA, University of Colorado, Boulder, Colorado 80309, USA*

Abstract

Zircon is a common accessory mineral in igneous rocks, including carbonatite-nordmarkite complexes. Zircons can record radiation damage and hydrothermal alteration through changes in oxygen isotope values, crystal structures, and geochemical and petrographic characteristics. The Mianning-Dechang rare earth element (REE) belt in China hosts 12 carbonatite-nordmarkite complexes and related Cenozoic REE deposits. We investigated zircons from these nordmarkites to understand the formation of the REE deposits. Three types of zircon from fresh and altered nordmarkite were identified. Type I zircons are unaltered, type II zircons experienced fenitization associated with hydrothermal alteration, and type III zircons were strongly affected by ore-forming fluids and REE mineralization. Type III zircons have higher Th, U, light REE, and REE contents (43,100, 52,000, 7,420, and 9,000 ppm, respectively) than type I zircons (1,450, 8,100, 265, and 1,130 ppm, respectively) and type II zircons (1,370, 19,520, 334, and 1,210 ppm, respectively). Petrographic observations, Raman spectra, and geochemical characteristics show that from type I to III zircons the crystals experienced increased radiation damage, hydrothermal alteration, and metasomatism by ore-forming fluids and show a transition to hydrothermal zircon. Type I, type II, and type III zircons have D_α^T (alpha dose) values of 0.6 to 29.5, 7.1 to 207, and 64 to 687 α-decay events/mg, with averages of 12.7, 87.36, and 144 α-decay events/mg, respectively. In general, the radiation damage trend shows that the Raman frequency is ~995 cm^{-1}, even at high levels of radiation damage. However, the Raman frequency of type III zircon can reach 991 cm^{-1} with a line width of 28 cm^{-1}, indicating type III zircons have a lower degree of crystallinity than type I and II zircons as a result of the effects of additional alteration by ore-forming fluids rich in Th and U. The involvement of ore-forming fluids and influx of meteoric water into the magmatic water is evident from the $\delta^{18}O$ values of type I, II, and III zircons of 5.15 to 8.65‰, 1.50 to 6.24‰, and 1.92 to 5.86‰, respectively. U-Pb dating of type I zircons yields similar ages within a given deposit. Type II and III zircons could not be dated for the formation ages of REE deposits due to their high degree of alteration, abundant mineral inclusions, and variable common and radiogenic Pb contents. Given the chemical composition of the hydrothermal fluids and REE minerals, the geochemical characteristics of type III zircons suggest that highly evolved ore-forming fluids rich in Na, K, Ca, Cl, SO_4, F, REEs, Th, U, Zr, Hf, and Pb facilitated zircon alteration. It is therefore concluded that the changes in zircon geochemistry and crystal characteristics could serve as a proxy for carbonatite-nordmarkite–related REE mineralization processes and as an indicator for REE exploration. A schematic model of the formation of type I, II, and III zircons and REE mineralization stages in the Mianning-Dechang REE deposits is presented.

Introduction

Zircon is a common accessory mineral that occurs widely in igneous, metamorphic, sedimentary, and metasomatic rocks. During its formation, zircon can incorporate modest amounts of U and Th into its crystal structure but excludes Pb, which makes it an excellent U-Th-Pb geochronometer (Harley et al., 2007). Advances in secondary ion mass spectrometry (SIMS) and multicollector-laser ablation-inductively coupled plasma-mass spectrometry (MC-LA-ICP-MS) have made it possible to determine the O and Hf isotopes of zircon with high spatial resolution, making zircon a robust mineral for assessing magma sources and crustal evolution (Cavosie et al., 2007; Kemp et al., 2007; Harrison, 2009; Bouvier et al., 2012; Muñoz et al., 2012; Wang, X.L., et al., 2013, 2014; Ling et al., 2016; Wang, C.M., et al., 2017). In addition to U and Th, zircon also incorporates trace amounts of temperature- or process-sensitive trace elements, including the rare earth elements (REEs), Y, and Ti. Zircon can thus also provide chemical evidence of the nature of mineral-melt-fluid processes during crust formation and maturation, hydrothermal alteration, and ore mineralization (Geisler et al., 2007; Hanchar and Van Westrenen, 2007; Harley et al., 2007). In addition, some zircons have both magmatic and hydrothermal origins when associated with various types of ore, such as Zr, Ta, REEs, Ti, Cu, W, or Sn (Yang, W.B., et al., 2014; Liu et al., 2015a; Lv et al., 2016; Wang et al., 2016; Li and Zhou, 2018). Therefore,

†Corresponding author: e-mail, ly@cags.ac.cn

ISSN 0361-0128; doi:10.5382/econgeo.4660; 26 p.
Digital appendices are available in the online Supplements section.
Submitted: July 29, 2018 / Accepted: May 8, 2019

zircon is widely considered as a reliable recorder of various geologic processes.

Zirconium has generally been regarded as an inert element in hydrothermal fluids, and zircon has been assumed to be resistant to hydrothermal alteration (Harley and Kelly, 2007). However, recent studies have shown that zircon might be susceptible to fluid-induced alteration, during which U-Th-Pb isotopes, oxygen isotopes, and trace elements within zircon could be mobilized (e.g., Putnis and Austrheim, 2010; Yang, W.B., et al., 2014; Li and Zhou, 2015; Takehara et al., 2018). This raises questions about traditional interpretations of petrographic characteristics, and elemental and isotopic data, from zircons that have experienced hydrothermal or mineralization-related alteration.

In this research, we investigated the petrographic characteristics, morphology, and crystal structure, as well as compositional and isotopic changes, of zircons during hydrothermal and mineralization-related alteration. This study focused on carbonatite-nordmarkite complexes in the Mianning-Dechang REE belt of southwestern China, which contains several Cenozoic (27–12 Ma) hydrothermal REE deposits that are genetically associated with mantle-derived carbonatite-nordmarkite complexes (Hou and Zhang, 2015; Hou et al., 2015; Tian et al., 2015). Notably, many of the magmatic zircons in the nordmarkites have been altered during fenitization and the later hydrothermal REE mineralization event. These deposits also provide an opportunity to study the evolution of ore-forming fluids and REE mineralization. We present petrographic observations (including the extent of radiation-induced lattice alteration), major and trace element data, laser Raman data, O isotope data, and U-Pb ages for both fresh and various types of altered zircon from the Mianning-Dechang REE belt. Using these data, we constrain the chemical, crystal structure, and isotopic changes that occur during zircon alteration and the nature of the alteration fluids. We also discuss the implications of our results for understanding carbonatite-nordmarkite–related REE mineralization and ore exploration.

Geology of the REE Deposits in the Mianning-Dechang REE Belt

The Mianning-Dechang REE belt is located in western Sichuan Province, southwest China, and is 270 km long and 15 km wide. A NS-trending belt of carbonatite-nordmarkite complexes (Fig. 1), bounded by the Yalongjiang and Anninghe strike-slip faults, intrudes Proterozoic crystalline basement rocks and Paleozoic-Mesozoic sedimentary sequences. In an individual complex, carbonatites occur as sills, dikes, stocks, and hypabyssal intrusions within the nordmarkite intrusions. The belt hosts the Maoniuping, Muluozhai, Lizhuang, and Dalucao REE deposits (Fig. 2) and contains a total estimated resource of over 3 million tons (Mt) of light rare earth oxides (REOs) (Hou et al., 2009).

Cenozoic strike-slip faults along the western margin of the Yangtze craton are associated with India-Asia continental collision (Guo et al., 2005) (Fig. 1A). These strike-slip faults cut the carbonatite-nordmarkite complexes, which are the main hosts of the hydrothermal REE deposits (Fig. 1B).

The carbonatites were likely formed by melting of the subcontinental lithospheric mantle (SCLM), which was previously metasomatized by high-flux REE- and CO_2-rich fluids derived from subducted marine sediments (Hou et al., 2015). The fertility of these carbonatites was related to the release of REEs from recycled marine sediments and intensity of REE metasomatism of the SCLM. These fertile carbonatites are quite different from the barren carbonatites that originate directly from mantle plumes and the asthenospheric mantle (Hou et al., 2015). Furthermore, overlapping emplacement ages and similar Sr-Nd isotope compositions and trace element data for the carbonatites and the spatially associated nordmarkites imply that these two rock types formed through liquid immiscibility (Hou et al., 2006). High-temperature, REE-rich hydrothermal fluids exsolved from the carbonatite-nordmarkite complexes and later precipitated the REE deposits through a combination of fluid cooling, mixing, and phase separation. The following geologic settings of individual REE deposits are revised from those proposed by Liu and Hou (2017) and Liu et al. (2019).

Maoniuping deposit

The basement geology in the Maoniuping area comprises five major lithological units (Fig. 2A): (1) NS-trending granitic plutons (90 km long and 6–14 km wide) dated at 723.1 ± 8.8 Ma (Liu and Hou, 2017); (2) a rhyolitic succession with ages of 750 to 600 Ma; (3) a 1,100-m-thick sequence of metamorphosed Devonian-Permian clastic rocks, limestones, and flood basalts intruded by Mesozoic granite; (4) a 700-m-thick, coal-bearing Triassic sedimentary sequence that overlies the metamorphic rocks; and (5) a complex of nordmarkite stocks and carbonatite sills, which is ~1,400 m long and 260 to 350 m wide. The location of the Maoniuping carbonatite-nordmarkite complex is controlled by the Haha strike-slip fault, which is a secondary structure with respect to the Mianning-Dechang fault. The complex intrudes a granitic complex and associated rhyolitic rocks (711.8 ± 9.4 Ma) (Liu and Hou, 2017). Nordmarkite is the predominant lithology at Maoniuping and is the major host rock for REE mineralization (Yuan et al., 1995; Liu and Hou, 2017). The majority of the carbonatite bodies (referred to as sills in previous publications) are located in the northern part of the intrusion (Guangtoushan section) (Fig. 2A). These rocks are dominated by medium- to coarse-grained calcite (50–90 vol %), with subordinate aegirine-augite, alkali amphibole, K-feldspar, barite, and fluorite. Although the currently mined part of the deposit (Dagudao section) contains some carbonatite bodies, their proportion is relatively small. This section consists predominantly of quartz nordmarkite, which hosts a stockwork grading into multiple branching veins of variable thickness. Fenitization is evident as mica-, sodic clinopyroxene-, and amphibole-rich zones and is prominent at Dagudao, where it is spatially associated with REE mineralization (Fig. 3B).

Maoniuping vein system: In contrast to the other deposits in the Mianning-Dechang REE belt, the REE ores at Maoniuping are hosted by a structurally complex system of mineralized veins, veinlets, and stockwork zones, which has an S-like outline in plan view and extends broadly in a north-northeast–south-southwest direction (Fig. 2A). This configuration suggests that the mineralization was controlled by strike-slip faulting. A total of 71 orebodies have been identified by drilling and assaying, ranging in size from 10 to 1,168 m in length

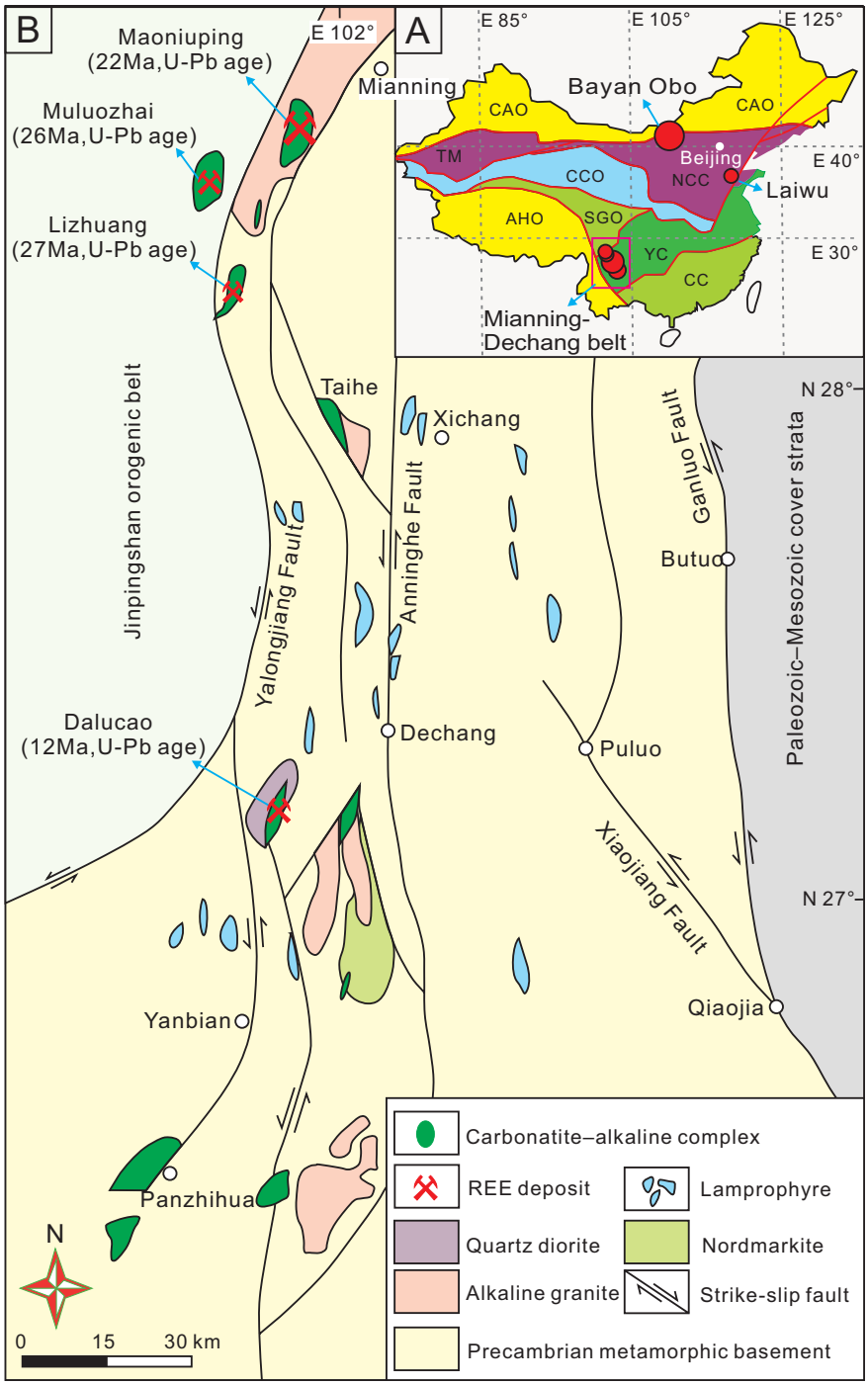

Fig. 1. Location, geology, and tectonics of the Maoniuping, Muluozhai, Lizhuang, and Dalucao REE deposits. (A) Overview of the tectonic regions of China. AHO = Alps-Himalaya orogeny, CAO = Central Asia orogeny, CC = Cathaysia craton, CCO = Central China orogeny, NCC = North China craton, SGO = Songpan-Ganze orogeny, TM = Tarim block, YC = Yangtze craton. (B) Geologic map showing the distribution of Cenozoic carbonatite-alkaline complexes in western Sichuan and the locations of reactivated faults, showing that the faults cut the nordmarkite and carbonatite bodies (modified after Yuan et al., 1995; Hou et al., 2015).

and 1.2 to 32 m in thickness (Yuan et al., 1995). The orebodies dip steeply toward the northwest at 65° to 80° and vary from massive to complexly zoned and to pod- or pocket-like mineralized structures. Most veins in the Dagudao section are hosted in fine- to medium-grained quartz nordmarkites. Geologic cross sections along a series of exploration lines, constructed on the basis of drill core data, suggest that the Dagudao section is the high-grade area of the Maoniuping deposit (Yuan et al., 1995). Drilling reveals that the base of the mineralized section occurs 150 m below the surface.

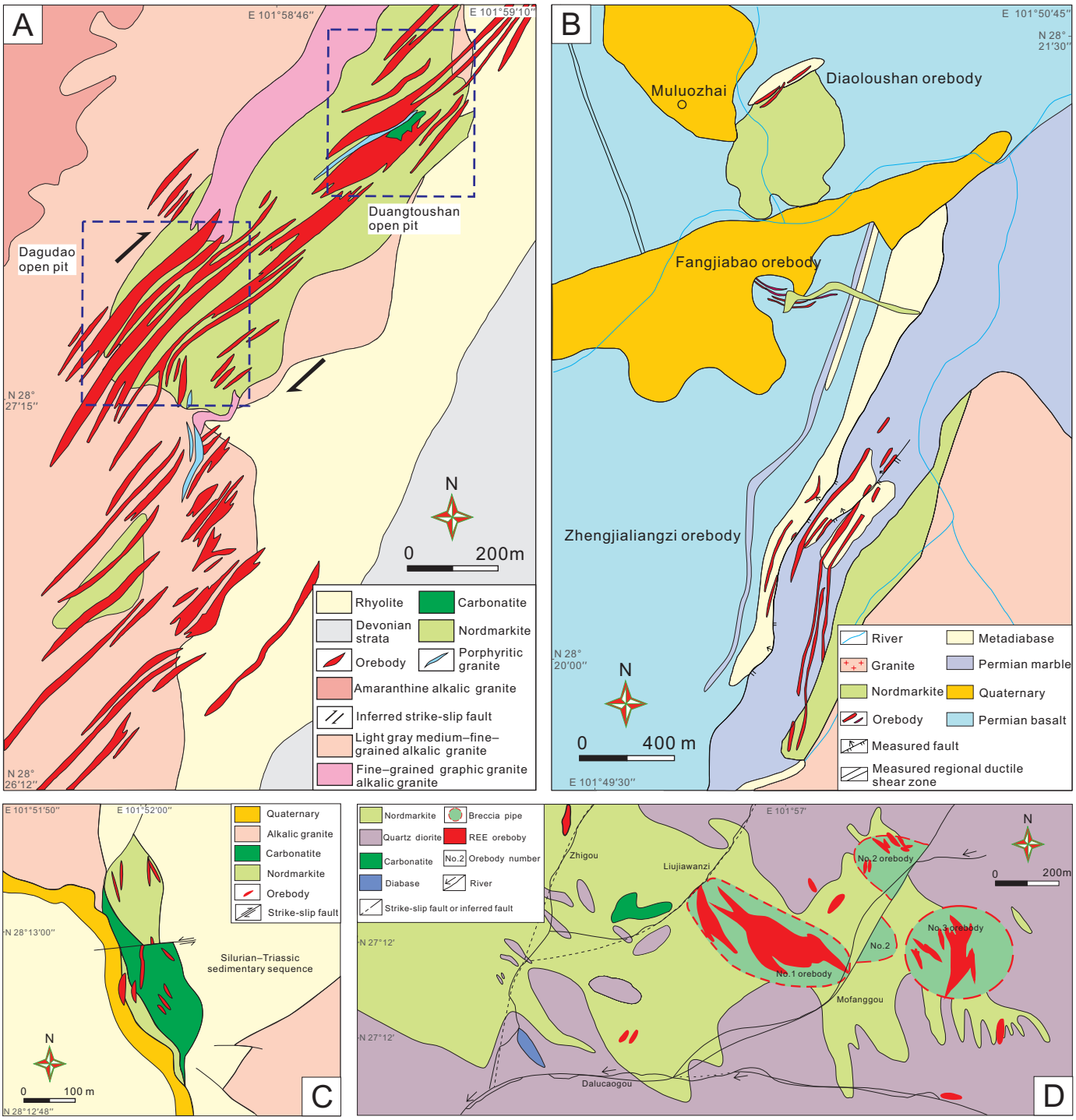

Fig. 2. (A) Simplified geologic map showing the distribution of carbonatite-alkaline complexes and associated REE orebodies within the Maoniuping deposit (modified from Hou et al., 2009). (B) Geologic map of the Muluozhai ore district (Institute of Multipurpose Utilization of Mineral Resources, Chinese Academy of Geological Sciences, unpub. data, 2008). (C) Schematic geologic map showing the key features of the nordmarkite-carbonatite complex and associated REE orebodies within the Lizhuang deposit (modified from Hou et al., 2009). (D) Geologic map showing the key features of the nordmarkite-carbonatite complex and associated REE orebodies within the Dalucao deposit (modified from Yang, unpub. data, 1998).

In previous studies (e.g., Yuan et al., 1995), the mineralized veins were categorized into five types based on morphology and mineralogy. However, this classification relied on the limited field evidence that was available at that time (i.e., prior to the excavation of the Dagudao open-pit mine). In recent years, outcrop exposure has much improved due to the mining, which enables us to revise the old classification and proposals regarding the structure of the vein system. In the previous

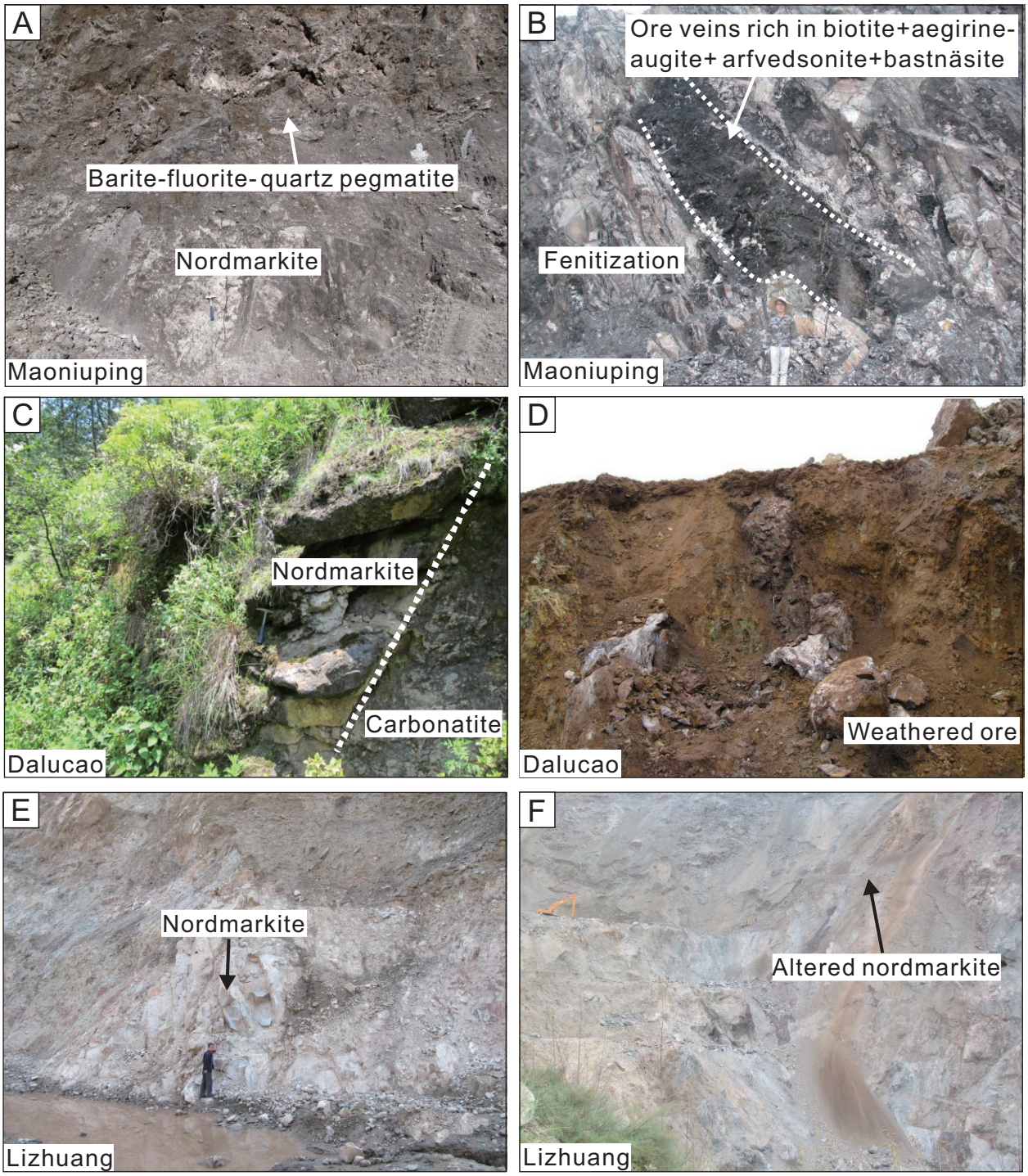

Fig. 3. Outcrop photographs of nordmarkite. (A) Barite-fluorite-quartz vein in nordmarkite, Maoniuping deposit (modified from Liu et al., 2015a). (B) Biotite-aegirine-augite-arfvedsonite-bastnäsite–bearing ore veins, Maoniuping deposit (modified from Liu and Hou, 2017). (C) Nordmarkite from orebody No. 1, Dalucao deposit, showing crosscutting, coarse-grained, barite-fluorite-quartz veins (modified from Liu and Hou, 2017). (D) Weathered ores from orebody No. 1, Dalucao deposit. (E) Fresh nordmarkite, lower Lizhuang deposit (modified from Liu and Hou, 2017). (F) Altered nordmarkite, Lizhuang deposit (modified from Liu et al., 2015a).

study (Liu et al., 2019), we identified three distinct units within the Dagudao section, each characterized by specific vein types, mineralogies, and ore potential. Transitions between these units are gradational. The top unit (~80 m thick) is the major source of high-grade REE ores and contains swarms of mineralized veins concentrated within the core area of the complex. The veins can be classified into four visually distinct types, all containing bastnäsite, on the basis of their predominant

coarse-grained mineral(s) and structure: (1) calcite veins, also containing sodic amphibole and clinopyroxene, barite, fluorite (colorless, purple, and green varieties), and minor sulfides (mainly galena); (2) sodic clinopyroxene veins, also containing sodic amphibole, fluorite (colorless and purple), and barite; (3) K-feldspar veins, with subordinate sodic clinopyroxene, barite, and quartz; and (4) micaceous veins.

Most of the veins are 15 to 30 cm wide (locally 12 m) and show a clear zoned structure. From the contact with the wall-rock nordmarkite inward, the following five zones are recognized: (1) mica of generation 1 (biotite, usually thinner than 2 cm); (2) K-feldspar; (3) sodic clinopyroxene; (4) sodic amphibole (partially replacing clinopyroxene); and (5) an axial zone comprising colorless to purple fluorite (±mica of generation 2 [fluorophlogopite], quartz, calcite, and barite), with occasional clusters of bastnäsite crystals, galena, and other sulfides. All the veins are modally zoned, but all five zones may not be present in a given vein.

Thick veins do not occur in isolation and are commonly accompanied by sets of subparallel and intersecting thinner veinlets and brecciation zones. These are particularly common in the southeastern part of the Dagudao section (i.e., downdip from the core area). Breccias are composed of angular wall-rock nordmarkite clasts in a matrix of ferromagnesian silicates (predominantly sodic clinopyroxene and amphibole). Locally, pervasively fenitized older metamorphic rocks are also present as clasts. Adjacent to the vein system, the wall-rock nordmarkite exhibits conspicuous jointing, which is broadly parallel to the major veins, and some of the joints are filled with very fine grained ferromagnesian silicates.

The bottom unit is mainly a dense stockwork of veinlets of widths typically not exceeding 1 cm. They are composed predominantly of fine- to medium-grained aegirine-augite, biotite, K-feldspar, albite, and quartz. Here, fluorite, barite, and bastnäsite are not nearly as common as in the top unit, and modal variations do not follow any discernible pattern. The middle unit (~50 m in thickness) is mineralogically and structurally transitional between the top and bottom units. Unlike the latter, it contains sodic amphibole developed after sodic clinopyroxene. Here, the vein thickness increases upward, but most of the veins are <3 cm wide.

Muluozhai deposit

The Muluozhai REE deposit is divided into the Diaoloushan and Zhengjialiangzi areas, which contain six main orebodies. The deposit is located in the northern Mianning-Dechang REE belt and is controlled by the strike-slip Yalongjiang fault, which connects with the Xianshuihe fault to the north. There are five main lithological units in the Muluozhai ore district (Fig. 2B): (1) Cenozoic nordmarkite that is the main host rock for REE mineralization and is associated with the Zhengjialiangzi, Diaoloushan, and Fangjiabao orebodies; (2) Cenozoic or Mesozoic granitic porphyries and alkali granites in the southeast; and (3) metadiabase that is located between (4) Permian basalt and (5) Permian limestone (marble), all of which were intruded by the nordmarkite during the Cenozoic. The Permian units are part of a thick sequence of Permian-Triassic marble and basalt, along with minor sandstone and other clastic sediments. The REE mineralization is hosted in veins and veinlets along the fractured contact between the metadiabase and nordmarkite or marble.

Drilling and assaying have been used to define the extent of most of the orebodies at Muluozhai. The Fangjiabao district hosts five orebodies, each 150 to 240 m long and <2 m thick.

Lizhuang deposit

The Lizhuang carbonatite-nordmarkite complex intrudes metamorphosed Silurian-Triassic clastic and carbonate rocks (Fig. 2C). The complex is 100 to 150 m wide, 400 m long, and consists of NNW-SSE–striking carbonatite sills and a nordmarkite pluton. The main REE orebody is elongate parallel to the contact zone between the carbonatite-nordmarkite complex and surrounding wall rocks. The principal ore mineral is bastnäsite, which formed synchronously with the alteration of the carbonatite-nordmarkite complex (Fig. 3E). In contrast to the other deposits in the Mianning-Dechang REE belt, ore mineralization was found in nordmarkite and carbonatite in the Lizhuang deposit (Fig. 3F).

The Lizhuang deposit comprises massive fluorite-quartz-calcite-bastnäsite ores and minor brecciated ores. The individual orebodies are 30 to 100 m long and 2.2 to 11.6 m thick (Fig. 2C). There are four types of ore: yellow banded, stockwork, black brecciated, and the principal brown-colored disseminated ore.

Unlike the Maoniuping and Muluozhai deposits, clear alteration of carbonatite and nordmarkite in the Lizhuang deposit was identified, evident as a red-brown coloration. In fresh carbonatite, the calcite is mostly unaltered, and altered carbonatite contains a large amount of bastnäsite. The altered nordmarkite is dominated by feldspar, biotite, quartz, and plagioclase, with minor calcite, barite, celestite, and bastnäsite.

Dalucao deposit

The Dalucao deposit is the only deposit in the southern part of the Mianning-Dechang REE belt and contains three orebodies (Nos. 1–3; Fig. 2D). The No. 1 and No. 3 orebodies are hosted in breccia pipes within carbonatite-nordmarkite host rocks (Fig. 3C) and have similar grades of 1.0 to 4.5 wt % REOs. Both pipes are elliptical in plan view, with long axes of 200 to 400 m and short axes of 180 to 200 m. The pipes extend downward for >450 m. The REE mineralization was controlled by the Dalucao fault. Faulting and brecciation facilitated the circulation of ore-forming fluids and provided space for REE precipitation.

Despite multiple phases of brecciation (four events are recorded in each of the pipes), mineralized veins and ores are contained wholly within altered nordmarkite at Dalucao (Liu et al., 2015c). The ores are weathered, brecciated, and dominated by fine-grained REE minerals (Fig. 3D) (Liu et al., 2015b, c). Brecciated ores are the main ore type, and it is notable that coarse-grained REE minerals are rare in the Dalucao deposit. Clasts within the breccia pipes are dominantly of magmatic origin or are composed of carbonate minerals. Pyrite, fluorite, barite, celestite, muscovite, quartz, and REE minerals all occur throughout the matrix. In the No. 3 orebody, REE mineral-bearing hydrothermal carbonate veins crosscut the other breccias and represent another type of brecciated ore.

Zircon Petrography

In the carbonatite-nordmarkite complexes of the study area, the nordmarkite is composed of ~80% K-feldspar and albite, 5 to 10% quartz, 1 to 5% biotite, ~5% aegirine-augite, and ~5% arfvedsonite in all deposits. Accessory minerals include apatite, zircon, allanite, and bastnäsite. The carbonatite is composed of 80 to 90% calcite and small amounts of aegirine-augite, biotite, quartz, arfvedsonite, and microcline.

In the Guangtoushan orebody in the Maoniuping deposit, adjacent to the vein system, the wall-rock nordmarkite exhibits conspicuous jointing broadly parallel to the major veins; some of the joints are filled with very fine grained ferromagnesian silicates. Macroscopically, the nordmarkite appears fresh and shows little alteration. Under the microscope, rock-forming minerals in the nordmarkite exhibit little alteration, and only some feldspar crystals have alteration at their rims.

In the strongly altered nordmarkite of the Lizhuang deposit, albite and K-feldspar have experienced severe alteration, and small carbonate veinlets of bastnäsite, calcite, barite, and fluorite cut across igneous rock-forming minerals. In addition, some bastnäsite has formed and overprinted the altered igneous rock-forming minerals, and gangue minerals such as fluorite, barite, and calcite are present.

For this study, we extracted zircon crystals exhibiting various types of alteration from nordmarkites in the Maoniuping, Muluozhai, Lizhuang, and Dalucao deposits. We identified three types of zircon. Type I zircons are found in fresh nordmarkite from all four deposits (Fig. 4A, B); these nordmarkites are commonly found a few kilometers from the REE orebodies or in the deep parts of the deposits. The zircon crystals in all these deposits are interstitial to apatite, muscovite, albite, and feldspar. They are 70 to 200 μm wide, 200 to 400 μm long, and prismatic in shape and show oscillatory zoning in cathodoluminescence (CL) images (Fig. 5A, B). Most crystals have well-developed {101} pyramids and {100} prisms (Fig. 4A, B), similar to the morphology of high-temperature zircons from alkaline igneous rocks (Pupin, 1980; Belousova et al., 2002, 2006; Corfu et al., 2003). Magmatic apatite, albite, K-feldspar, and muscovite occur as inclusions in large (>5 μm) zircon crystals. Type I zircon crystals have a homogeneous texture in backscattered electron (BSE) images (Fig. 6A).

Type II zircons are found in nordmarkites adjacent to various types of REE mineralization and hydrothermal

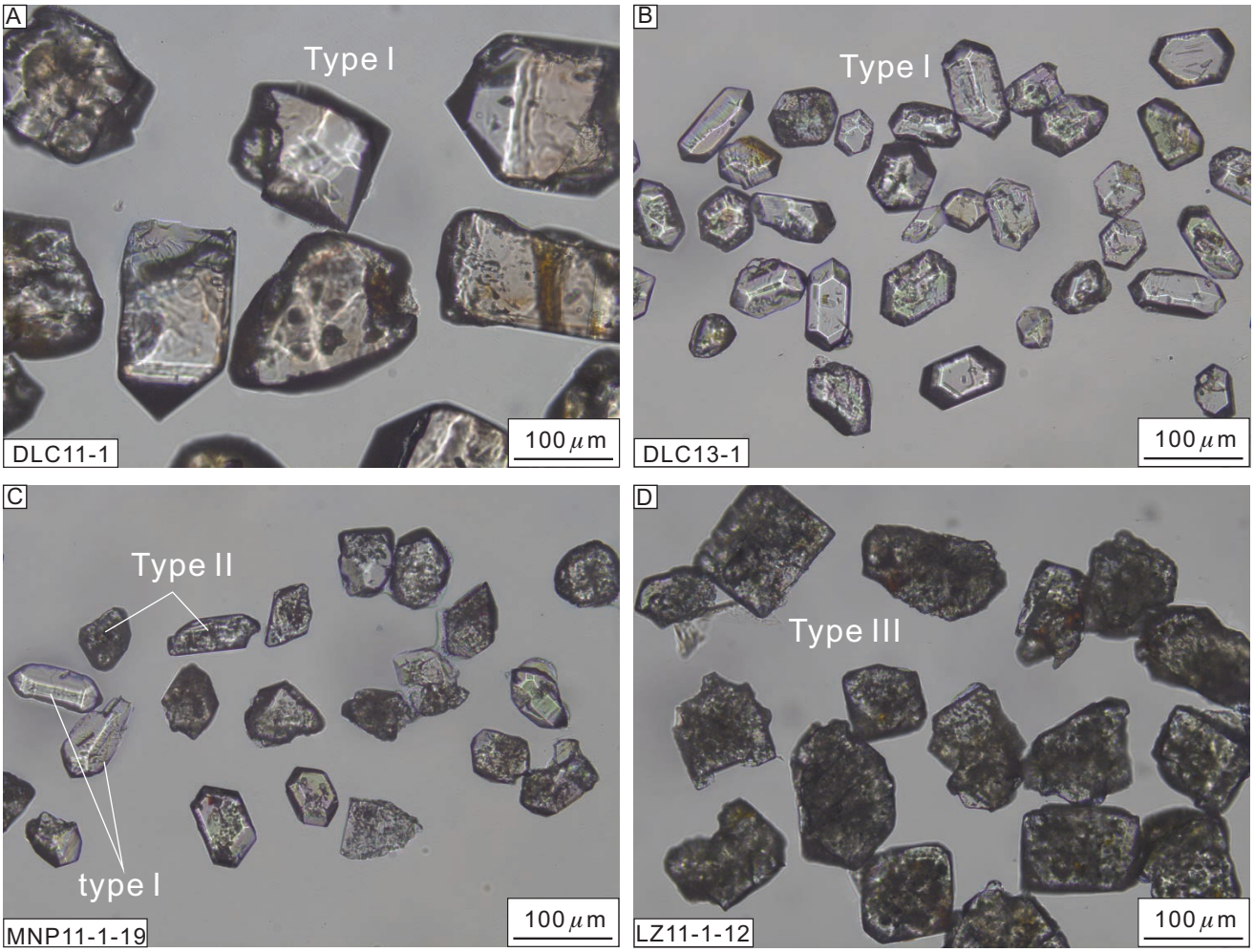

Fig. 4. Transmitted-light microscopic images of zircons from the Mianning-Dechang REE belt. (A, B) Type I zircons in nordmarkite. (C) Type II zircons in nordmarkite with a slightly dusty appearance. (D) Type III zircons in nordmarkite exhibiting heavy alteration and cloudy inner regions.

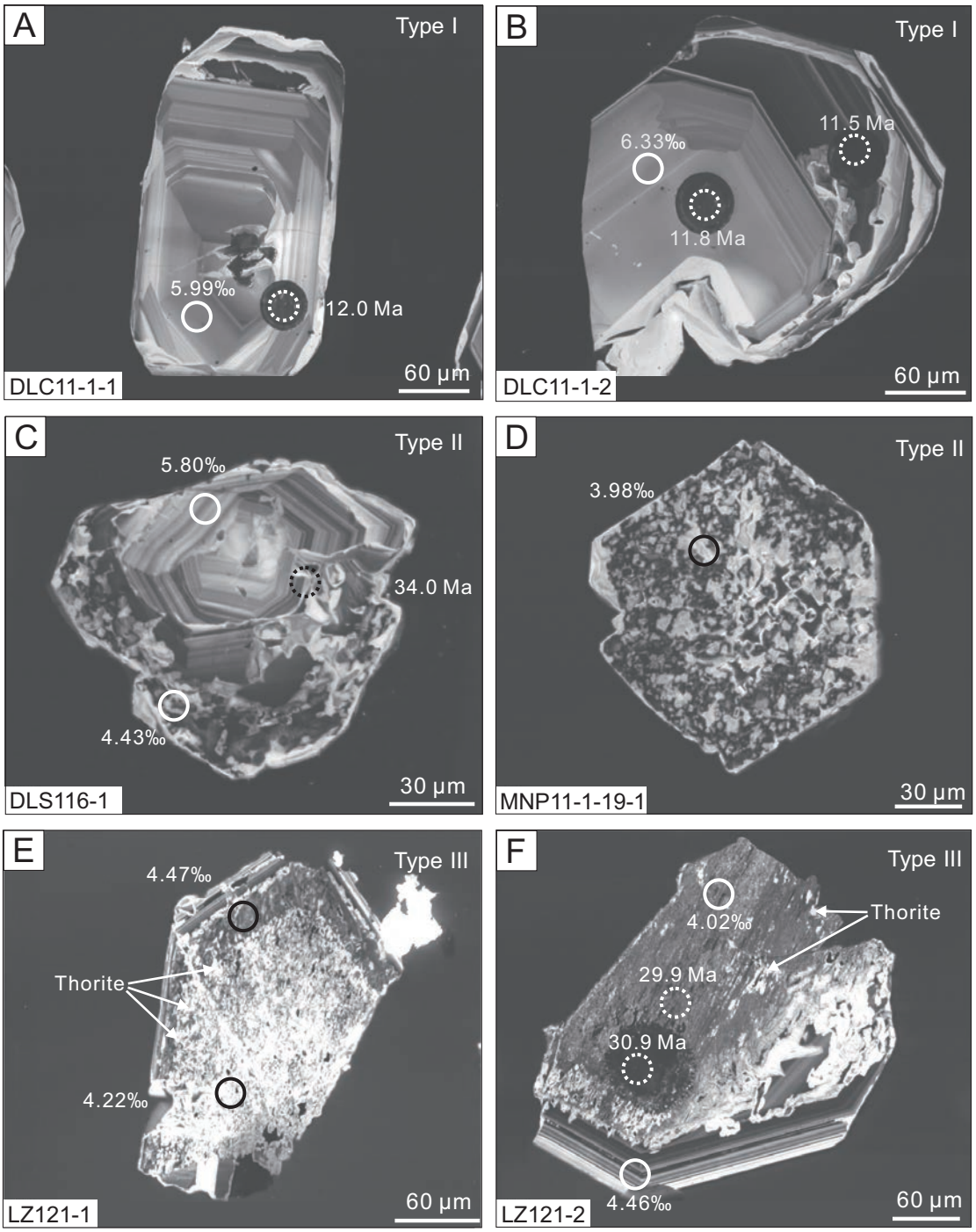

Fig. 5. Cathodoluminescence images of the zircons, annotated with SHRIMP U-Pb ages (dotted circle) and O isotope data (solid circle). (A, B) Type I zircon. (C) Type II zircon with obscure CL zoning. (D) Type II zircon without CL zoning. (E, F) Type III zircons containing inclusions of fine-grained thorite (D and E modified from Guo et al., 2017).

veins (Fig. 4C). These zircons are 50 to 150 μm wide, 100 to 300 μm long, euhedral to subhedral, and sometimes prismatic in shape. Under transmitted light, these zircons often have a mottled appearance (Fig. 4C). Many CL images show zircon cores with oscillatory zoning and rims with cloudy or irregular zoning (Fig. 5C). BSE imaging revealed differences in zircon structure, with an evenly textured core and a rim containing mineral inclusions (Fig. 6B). Gray domains occur along grain boundaries or lattice planes and as small patches randomly distributed across bright domains. Minor amounts of Th-rich phases occur as inclusions in the gray domains. Some irregularly dark and bright cores in the zircons are indicative of radiation damage (Corfu et al., 2003; Wang et al., 2014).

Type III zircons are found mainly in the REE-mineralized nordmarkite pluton in the Lizhuang deposit. They are 80 to

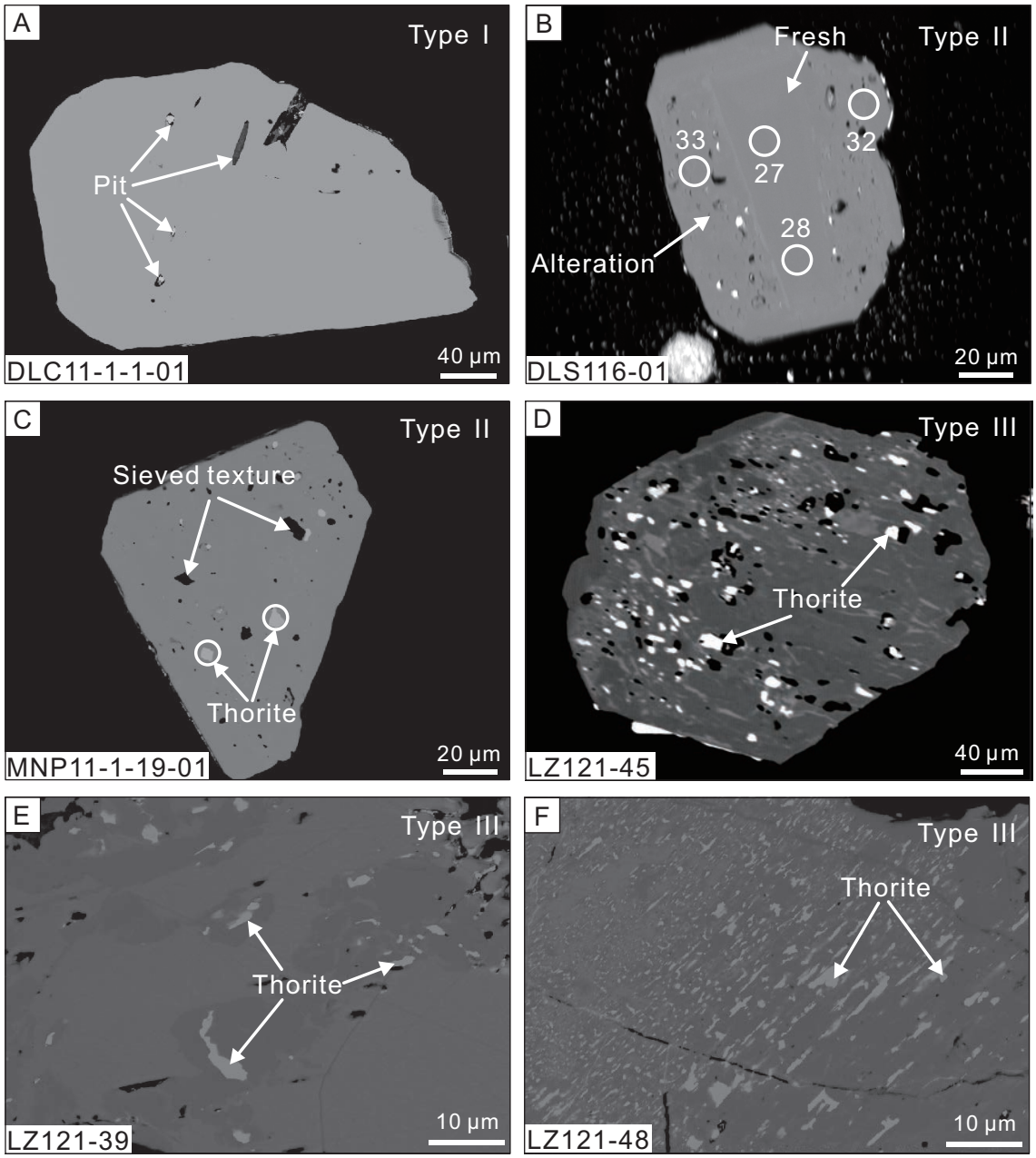

Fig. 6. BSE images of the zircons. (A) Type I zircon showing a chemically homogeneous interior. (B) Type II zircon with a chemically homogeneous interior and heterogeneous exterior. (C) An altered type II zircon showing an uneven structure and thorite mineral inclusions. (D) A small domain of the interior of a type III zircon displaying numerous fine-grained thorite grains with an irregular shape. (E, F) Thorite mineral inclusions in type III zircons.

200 μm wide, 160 to 200 μm long, and euhedral to anhedral. Under transmitted light, these zircons have a mottled appearance (Fig. 4D). CL imaging shows zircon crystals with patchy, cloudy, or very irregular zoning. Some crystals contain small oscillatory zones at the grain margins (Fig. 5E, F). BSE imaging of zircons shows bright and dark domains, with clear boundaries between the two domains. The development of these gray domains tends to be related to fluid pathways, commonly along grain rims, brittle fractures, or crystallographic lattice planes (Figs. 6F, 7). Dark BSE domains also occur as irregular intersecting patches throughout entire zircons grain (Figs. 6D, 7). Most dark BSE image domains contain abundant Th-rich inclusions, as well as minor barite, fluorite, and celestite inclusions (Fig. 6D-F). Type III zircon cores contain a dense distribution of fine (0.5–5.0 μm) thorite mineral inclusions. There are fewer thorite mineral inclusions toward the margin of the zircon grains, although these inclusions are larger (up to 40 μm; Fig. 6D-F). Most inclusions are anhedral and randomly distributed. Given these attributes, type III zircons appear to have experienced radiation damage and hydrothermal alteration and contain abundant secondary mineral inclusions (Fig. 7).

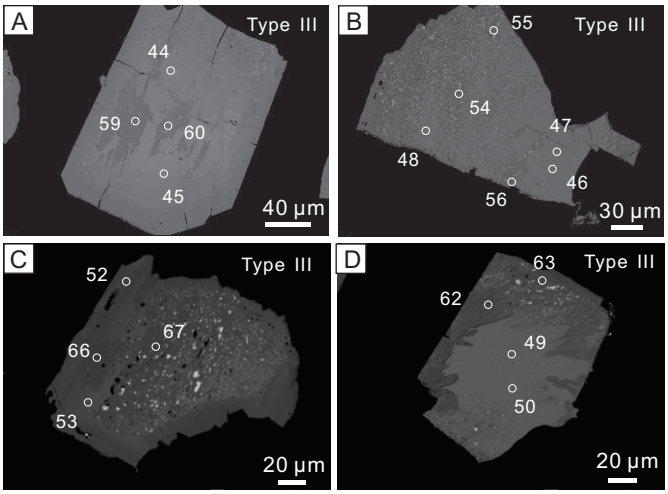

Fig. 7. BSE images of type III zircons and thorite and other mineral inclusions; gray and bright domains are affected by hydrothermal fluid alteration. The numbers correspond to Appendix Table A1.

Analytical Methods

Zircons were separated from fresh and altered nordmarkites from the Dalucao, Maoniuping, Lizhuang, and Diaoloushan deposits. Zircon grains were extracted using conventional procedures. Samples were crushed and sieved, followed by elutriation, drying, and separation of zircons by magnetic, electromagnetic, and heavy liquid methods. Zircons were handpicked under a binocular microscope and then mounted onto double-sided adhesive tape and enclosed in an epoxy resin disk with a diameter of 2.5 cm, along with TEMORA 1 reference zircon ($^{206}Pb/^{238}U$ age = 416.8 ± 1.3 Ma; Black et al., 2003; Nasdala et al., 2008). The morphology of the zircon crystals was examined in both transmitted and reflected light, and images were taken using an optical microscope and a CL imaging system. The CL images were acquired using a HITACHI S3000-N scanning electron microscope equipped with a Robinson BSE detector and Gatan Chroma CL imaging system. Zircon separation and CL imaging were all carried out at the Beijing SHRIMP Center, Chinese Academy of Geological Sciences (CAGS), Beijing, China.

Micro-Raman spectroscopy of zircon crystals was performed on a standard Raman microscope (LabRAM HR Evolution, Horiba) with a 100× objective lens (0.9 numerical aperture) and 0.21-mm working distance. We used a 633-nm and 4- to 5-mW laser with a beam focus size of ~1-μm diameter and spectral resolution of 1 cm^{-1}. Measurement times were 4 to 150 s per spectrum. Polarization and crystal orientation were rotated to maximize the Raman response, and spectra were normalized to compare relative intensities between different crystals. Spectral positions and line widths were extracted using Voigt line shape fitting (Fig. 8; Table 1).

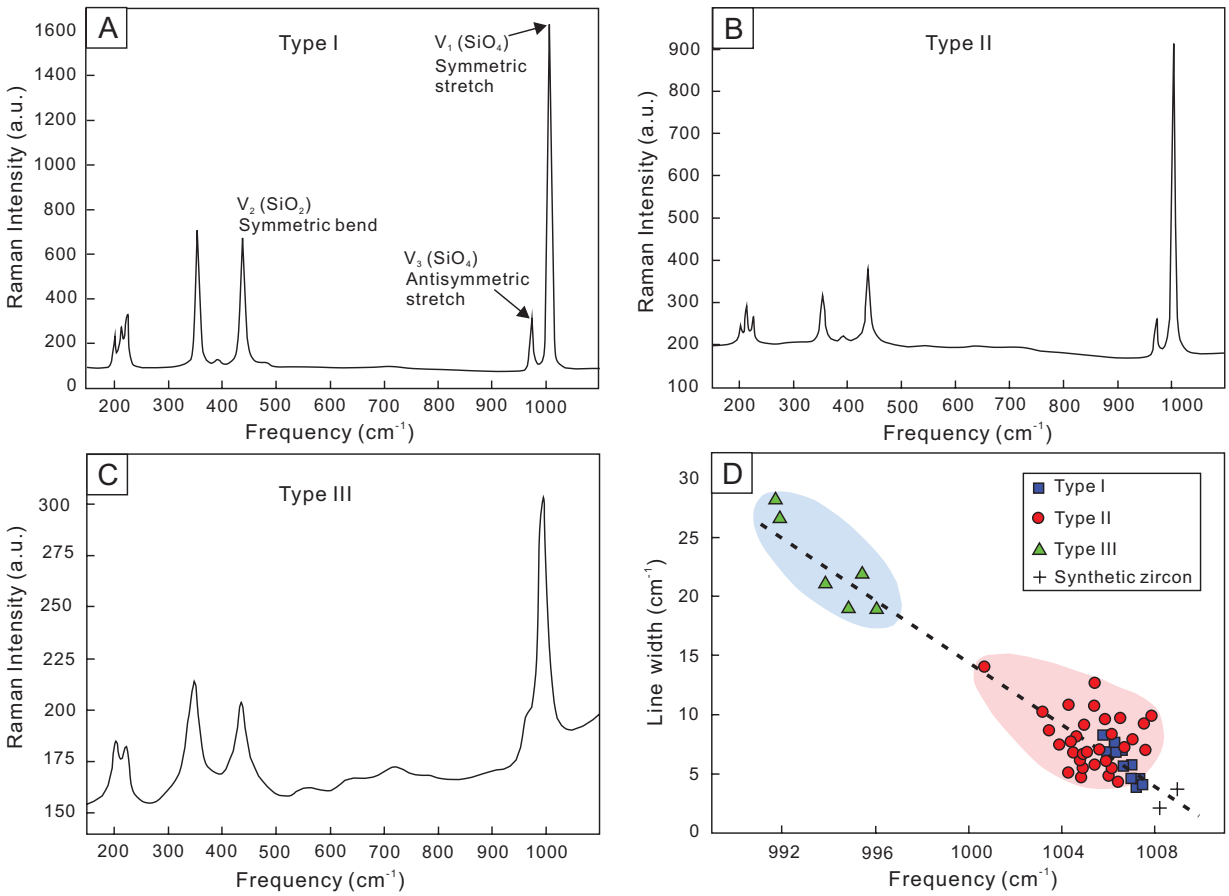

Fig. 8. Raman spectra for (A) type I (primary) zircons, (B) type II zircons, and (C) type III zircons. (D) Correlation between the full width at half maxima (FWHM) and peak frequency of the symmetric stretching mode of zircon.

Table 1. Raman Band Parameters of Representative Zircon Types from the Mianning-Dechang REE Belt

		E_g(tetrahedron rotation)		A_{1g}(symmetric bending, v_2)		B_{1g} (antisymmetric stretching, v_3)		
Form of zircons	Samples	v(cm^{-1})	I(counts · 10^4)	v(cm^{-1})	I(counts · 10^4)	v(cm^{-1})	FWHM	I(counts · 10^4)
Dalucao deposit								
Type I	DLC11-1-1	355.4	3.5	439.3	4.4	1,006.5	6.8	13.6
Type I	DLC11-1-2	359.4	2.5	439.8	2.5	1,006.2	7.7	1.2
Type I	DLC11-1-3	355.6	3.5	439.8	4.6	1,006.4	8.3	12.4
Type I	DLC11-2-3	357.5	3.2	439.8	3.4	1,008.1	9.2	10.2
Type I	DLC11-2-6	355.6	2.9	439.8	3.3	1,006.4	7.2	10.8
Maoniuping deposit								
Type I	MNP11-1-19-1	355.6	2.9	437.9	3.1	1,006.4	10.5	3.1
Type I	MNP11-1-19-4	353.8	2.7	437.9	2.9	1,004.6	8.6	3.5
Type I	MNP11-1-19-5	355.6	3.9	437.9	2.4	1,006.4	7.4	3.1
Type II	MNP11-1-19-2	353.8	2.4	437.9	2.8	1,004.6	9.8	6.4
Type II	MNP11-1-19-3	351.9	1.8	437.9	2.2	1,004.6	10.9	4.3
Type II	MNP11-1-19-6	351.9	2.8	437.9	4.1	1,004.6	8.4	8.8
Type II	MNP11-1-19-7	354.7	2.7	438.1	4.1	1,005.4	7.8	9.8
Lizhuang deposit								
Type I	LZ121-1	355.6	3.7	439.8	3.8	1,006.4	6.9	7.4
Type I	LZ121-2	353.6	5.2	439.3	6.4	1,004.6	11.2	12.6
Type III	LZ121-3	352.4	1.7	438.1	1.9	1,001.6	13.7	3.8
Type III	LZ121-4	352.4	2.2	438.1	2.4	999.3	17.6	4.1
Type III	LZ121-5	352.4	3.8	438.1	4.6	1,001.6	14.1	8.7
Type III	LZ121-6	354.7	2.1	438.1	1.8	1,005.1	13.9	2.1
Diaoloushan deposit								
Type I	DLS116-1	355.6	4.0	437.9	4.5	1,006.4	7.8	6.8
Type I	DLS116-2	355.6	3.2	437.9	3.8	1,004.6	9.1	5.0
Type I	DLS116-3	353.8	2.5	437.9	3.0	1,004.6	8.0	7.1
Type II	DLS116-4	351.9	3.5	437.9	4.3	1,004.6	8.4	9.3

Sample mounts (25 mm diam) for oxygen isotope analysis were made at the Beijing SHRIMP Center. Each $^{18}O/^{16}O$ analysis took ~7 min, including ~5 min of waiting for the isotopic composition to stabilize, during which the ion beam was tuned and baselines were measured, and 2 min of O isotope measurement. The analytical procedures and conditions were similar to those described by Ickert et al. (2008). The intensity of the Cs^+ primary ion beam was ~3 nA, producing secondary $^{16}O^-$ count rates above 10^9 cps. Spot diameters were ~35 μm. We used the TEMORA 2 zircon ($\delta^{18}O$ = 8.20‰; Black et al., 2004) as a reference material for calibration of instrumental mass fractionation, and this zircon was mounted together with our samples. The standard was analyzed two or three times at the start of each analytical session and then after every three sample analyses. Uncertainties on individual analyses presented in the table are shown as 2σ (Table 2).

We used a combination of CL images and optical microscopy to select the clearest and least fractured rims of zircon crystals as suitable targets for laser ablation trace element analysis. Trace element analyses were conducted by LA-ICP-MS. Sample mounts were placed in a special sample cell designed by Laurin Technic (Canberra, Australia) and flushed with Ar and He. Laser ablation was accomplished using a pulsed Resonetic 193-nm ArF excimer laser, operated at a constant energy of 80 mJ, with a repetition rate of 8 Hz and spot diameter of 31 μm. The ablated aerosol was carried to an Agilent 7500a ICP-MS by He gas via a Squid system to smooth signals (Liang et al., 2009; Tu et al., 2011). Data were acquired for 30 s with the laser off and 40 s with the laser on, giving ~100 mass scans. NIST SRM 610 glass (Pearce et al., 1997; Gao et al., 2002) and TEMORA zircon standards (Black et al., 2003) were used as external standards. We analyzed standards after every five samples. We used ICPMSDataCal to perform off-line inspection and integration of background and analyte signals, time-drift corrections, quantitative calibrations for trace element analyses, and U-Pb dating (Liu et al., 2008). Concordia diagrams and weighted-mean calculations were made using Isoplot /Ex_ver3 (Ludwig, 2003; Table 3).

Major element compositions of minerals were analyzed using a JXA-8230 electron microprobe at the Institute of Mineral Resources, CAGS (App. Table A1).

All U-Th-Pb analyses were conducted using a SHRIMP II instrument. TEMORA 1 was analyzed to estimate mass fractionation (Black et al., 2003). This reference sample was analyzed after every three sample analyses to monitor the stability of the instrument and ensure reliable results. Our instrumental conditions and measurement procedures were similar to those reported previously (Compston, 1992; Black et al., 2003; Stern and Amelin, 2003), including analyses undertaken in the same facility. We used a 5- to 7-nA primary O^{2-} ion beam to analyze 25- to 30-μm-diameter spots. We acquired five scans through nine mass stations for the standards, including $^{196}Zr_2O$, ^{204}Pb, background, ^{206}Pb, ^{207}Pb, ^{208}Pb, ^{238}U, ^{248}ThO, and ^{254}UO. Reference zircon M257 was analyzed for elemental abundance calibration. TEMORA 1 was analyzed for calibration of $^{206}Pb/^{238}U$ after every three or four analyses. Common Pb was corrected using measured ^{204}Pb abundances. Data reduction was performed using SQUID 1.0 (Ludwig, 2001)

Table 2. Oxygen Isotope Compositions of the Three Zircon Types in the Mianning-Dechang REE Deposits

Sample	Type	$\delta^{18}O$ (‰)	Error (‰)	Sample	Type	$\delta^{18}O$ (‰)	Error (‰)
Dalucao deposit				Lizhuang deposit			
DLC11-1-1-02	I	6.02	0.16	LZ121-20	III	3.70	0.40
DLC11-1-1-03	I	6.28	0.14	LZ121-09	III	3.89	0.17
DLC11-1-1-06	I	5.89	0.07	LZ11-1-12-01	III	3.90	0.11
DLC11-1-1-07	I	5.90	0.10	LZ121-03	III	3.90	0.07
DLC11-1-1-08	I	6.56	0.12	LZ121-02	III	4.02	0.21
DLC11-1-1-10	I	6.33	0.07	LZ11-1-12-04	III	4.10	0.09
DLC11-1-1-12	I	6.86	0.13	LZ121-08	III	4.19	0.09
DLC11-1-1-13	I	5.99	0.09	LZ121-12	III	4.22	0.40
DLC11-1-1-14	I	5.96	0.12	LZ121-04	III	4.39	0.18
DLC11-1-1-15	I	6.17	0.12	LZ121-06	III	4.46	0.12
DLC11-1-1-16	I	5.90	0.15	LZ121-14	III	4.62	0.35
DLC11-2-01	I	5.69	0.12	LZ121-11	III	4.74	0.23
DLC11-2-21	I	8.65	0.28	LZ121-17	III	5.15	0.51
				LZ121-10	III	5.26	0.15
Maoniuping deposit	I	5.15	0.17	LZ121-13	III	5.36	0.24
MNP11-1-19-02f	I	5.17	0.08	LZ121-16	III	5.51	0.12
MNP11-1-19-09f	I	5.39	0.07	LZ11-1-12-03	III	5.68	0.06
MNP11-1-19-11f							
MNP11-1-19-05f	I	5.51	0.11	Diaoloushan deposit			
MNP11-1-19-03f	I	5.52	0.17	DLS-116-27	I	5.23	0.08
MNP11-1-19-07f	I	5.71	0.07	DLS-116-02	I	5.34	0.10
MNP11-1-19-01al	II	4.00	0.17	DLS-116-12	I	5.40	0.12
MNP11-1-19-16al	II	1.50	0.15	DLS-116-04	I	5.78	0.11
MNP11-1-19-04al	II	3.13	0.16	DLS-116-18	I	5.80	0.10
MNP11-1-19-14al	II	3.34	0.08	DLS-116-19	I	5.80	0.09
MNP11-1-19-08al	II	3.67	0.18	DLS-116-06	I	5.87	0.11
MNP11-1-19-12al	II	3.85	0.11	DLS-116-01	I	5.88	0.11
MNP11-1-19-10al	II	3.98	0.08	DLS-116-17	I	5.93	0.06
MNP11-1-19-19al	II	5.13	0.11	DLS-116-07	I	6.00	0.10
MNP11-1-19-13al	II	6.19	0.11	DLS-116-15	I	6.04	0.11
MNP11-1-19-06al	II	6.24	0.14	DLS-116-13	I	6.06	0.11
				DLS-116-09	I	6.07	0.09
Lizhuang deposit	I	5.30	0.15	DLS-116-03	I	6.10	0.12
LZ121-05f	I	5.46	0.13	DLS-116-08	I	6.10	0.09
LZ121-24f	I	5.82	0.28	DLS-116-10	I	6.15	0.12
LZ121-22f	I	6.18	0.26	DLS-116-05	I	6.34	0.12
LZ121-23f	III	1.92	0.43	DLS-116-11	I	6.45	0.09
LZ121-21al	III	2.71	0.58	DLS-116-21	I	6.93	0.08
LZ11-1-12-07al	III	2.77	0.11	DLS-116-16	II	3.57	0.10
LZ121-25al	III	2.87	0.16	DLS-116-28	II	3.79	0.10
LZ121-07al	III	2.89	0.10	DLS-116-14	II	4.19	0.11
LZ121-18al	III	2.92	0.42	DLS-116-20al	II	4.43	0.10
LZ121-15al	III	3.52	0.21	DLS-116-24al	II	4.81	0.10
LZ11-1-12-05al	III	3.54	0.39	DLS-116-26al	II	5.34	0.04
LZ121-19al	III	3.57	0.09	DLS-116-23al	II	5.38	0.14
LZ11-1-12-06al				DLS-116-25al	II	5.68	0.11
				DLS-116-22al	II	5.81	0.12

Abbreviations: al = altered, f = fresh

and ISOPLOT/Ex software (Ludwig, 2003). Young zircons (<800 Ma) have only small amounts of ^{207}Pb, giving low count rates and high analytical uncertainties; therefore, age determination for young zircons is based primarily on $^{206}Pb/^{238}U$ ratios (App. Table A2). Errors in individual analyses are based on counting statistics and are quoted at the 1σ level; those for pooled analyses are quoted at the 2σ level.

Whole-rock geochemical analyses of fresh nordmarkite, nordmarkite after fenitization, and nordmarkite after REE mineralization were performed at the National Research Center of Geoanalysis, CAGS. Whole-rock powder samples (0.7 g) were mixed with 5.3 g $Li_2B_4O_7$, 0.4 g LiF, and 0.3 g NH_4NO_3 in a 25-mL porcelain crucible. The powder mixture was transferred to a Pt alloy crucible, 1 mL of LiBr solution was added to the crucible, and the sample was then dried. The sample was then melted in an automatic fusion machine and the resulting cooled glass was used for the X-ray fluorescence (XRF) major element analyses. Major elements were analyzed by inductively coupled plasma-atomic emission spectrometry (ICP-AES). The analytical precisions are better than 1% relative standard deviation (RSD) for values higher than 1 wt % and 5% RSD for values lower than 1 wt %.

For the complete digestion of refractory minerals such as zircons in whole-rock geochemical analyses, Li tetraborate flux fusion is adopted. The following procedure was adopted for trace element analyses of fresh nordmarkite, nordmarkite after fenitization, and nordmarkite after REE mineralization in REE deposits from the Mianning-Dechang REE belt,

based on the procedure of the State Standard of the People's Republic of China (GB) (Standardization Administration of China, 2010). For analyses of trace elements, whole-rock powder samples (50 mg) were dissolved in distilled 1 mL HF and 0.5 mL HNO_3 in 15 mL Savillex Teflon screw-cap capsules at 190°C for 1 d, dried, digested with 0.5 mL HNO_3, and then dried again. The capsule content was then digested with 0.5 mL HNO_3 and dried again to ensure complete digestion. The sample was then digested with 5 mL HNO_3 and sealed at 130°C in an oven for 3 h. After cooling, the solution was transferred to a plastic bottle and diluted to 50 mL before analysis. The sample solutions were analyzed for trace elements by ICP-MS. To verify the data accuracy, several standards (GBW 07120, GBW 07103, GBW 07105, and GBW 07187) were analyzed together with the samples (App. Table A3). The analytical precision for most elements is generally better than 5% RSD, as assessed by the reproducibility of standard measurements.

Results

Micro-Raman spectroscopy

We conducted micro-Raman spectroscopic analysis on different types of zircon from the different localities. We followed established methods by restricting the analysis to the prominent ν_3 antisymmetric stretching mode at 1,008 cm^{-1} of B_{1g} symmetry. We determined line widths and peak positions from Voigt profile fitting.

We observed three distinct spectral characteristics (Fig. 8) corresponding mainly to the three types of zircon (I, II, and III) described above. The zircon crystals are highly heterogeneous on the micron scale and show varying degrees of alteration (from unaltered to strongly altered), even within a single crystal. Raman point spectra were selected to represent the dominant phase in each crystal.

Figure 8A shows typical spectra from primary zircons (type I and unaltered regions of type II and III zircons), which are characterized by narrow peaks and a low photoluminescent background. There is a narrow distribution in peak position, ranging from 1,006 to 1,007.5 cm^{-1}, with correlated changes in line width from 4 to 8 cm^{-1} (Fig. 8D; blue squares).

We observed an increase in fluorescent background with progressive alteration, together with a decrease in Raman peak intensity, and an increase in line width and continuous redshift of the ν_3 resonance frequency in typical spectra for type II and III zircons (Fig. 8B, C). Some crystals are dominated by regions that exhibit a larger redshift (1,003–1,006.5 cm^{-1}) yet maintain a relatively narrow line width. This characteristic is most common for type II crystals (red circles in Fig. 8D). Some other zircon crystals are dominated by regions that exhibit broad peaks (7–13 cm^{-1}), while maintaining a high resonance frequency (1,004–1,008 cm^{-1}). This observation is most common for highly altered zircons and parts of type III zircons. We observed a third group, exclusive to type III zircons, with regions that show strong fluorescence and a weak Raman signal (Fig. 8C), with broad peaks (18–30 cm^{-1}), large redshift (990–996 cm^{-1}), and a wide range of values (Fig. 8D; green triangles).

The general trend of increasing line width and decreasing peak position is characteristic of a decrease in the degree of crystallinity (Geisler et al., 2001a, b), possibly due to defects and amorphous regions within the crystal lattice, which result in phonon softening and increased damping, typically associated with radiation damage (Banik et al., 2017). The observed trend is in good agreement with the results from BSE and CL imaging.

Chemical composition of the zircons and their mineral inclusions

Electron microprobe analysis shows that type I zircons have uniformly high SiO_2 (31.78–33.02 wt %) and ZrO_2 (62.03–64.02 wt %) contents, together with minor amounts of UO_2 (0.02–1.38 wt %), ThO_2 (0.09–0.55 wt %), HfO_2 (0.28–1.81 wt %), Ce_2O_3 (below detection limit to 0.33 wt %), and REE_2O_3 (0.37–1.07 wt %) (App. Table A1). Type I zircons all have similar chondrite-normalized REE patterns (Fig. 9). The light REE (LREE) contents vary from 56 to 1,167 ppm, and the total REE contents from 340 to 2,386 ppm (Table 3).

Type II zircons also have homogeneous chemical compositions but higher concentrations of UO_2 (<1.64 wt %), ThO_2 (0.00–0.71 wt %), HfO_2 (0.32–2.69 wt %), Ce_2O_3 (<0.17 wt %), and REE_2O_3 (0.41–0.99 wt %) (App. Table A1). The altered regions of type II zircons all have similar chondrite-normalized REE patterns (Fig. 9B). The LREE contents of type II zircons vary from 151 to 2,284 ppm, and the total REE contents vary from 904 to 3,394 ppm (Fig. 9; Table 3). Type III zircons contain numerous mineral inclusions, and gray domains in type III zircons contain 0.08 to 2.56 wt % UO_2, 0.08 to 15.03 wt % ThO_2, 0.33 to 1.87 wt % HfO_2, 0.02 to 0.95 wt % Ce_2O_3, and 0.21 to 2.41 wt % REOs. Bright domains in type III zircons contain 1.20 to 3.50 wt % UO_2, 1.14 to 11.78 wt % ThO_2, 0.62 to 1.77 wt % HfO_2, <0.63 wt % Ce_2O_3, and 0.79 to 1.83 wt % REOs (App. Table A1). In type III zircons, the bright domains have higher concentrations of UO_2, ThO_2, HfO_2, Ce_2O_3, and REOs than the gray domains.

U-Pb ages

In previous studies, U-Pb dating was performed only on type I zircons (Liu et al., 2015a; Ling et al., 2016). In this study, type II and III zircons were also analyzed (Fig. 10). We obtained U-Pb ages for type I zircons from the Dalucao, Maoniuping, Lizhuang, and Diaoloushan deposits of 14 to 9, 31 to 26, 28 to 26, and 32 to 27 Ma, respectively (App. Table A2). The altered parts of type II zircons from the Maoniuping (25–20 Ma) and Muluozhai (28–25 Ma) deposits have slightly younger ages than type I zircons from the same deposit (Fig. 10B, D). In the Lizhuang deposit, altered parts of type III zircons yielded ages of 37 to 31 Ma, which is older than unaltered type I zircons (28–26 Ma) from the same deposit (App. Table A2). Therefore, type II and III zircons from altered nordmarkite are not suitable for U-Th-Pb dating, particularly in the case of type III zircons. It is proposed that minerals such as arfvedsonite, muscovite, bastnäsite, monazite, xenotime, or titanite might be better chronometers for these rocks (Ling et al., 2016).

Zircon O isotope data

The $\delta^{18}O$ values show a progressive decrease from type I to II to III zircons (Fig. 11). Type I zircons have $\delta^{18}O$ values of 5.15 to 8.65‰. The altered parts of type II zircons have $\delta^{18}O$

Table 3. LA-ICP-MS Trace Element Analyses (ppm) of the Three Zircon Types in the Mianning-Dechang REE Deposits

Sample	Type	P	Ca	Ti	Y	La	Ce	Pr	Nd	Sm	Eu	Gd	Tb	Dy	Ho	Er	Tm
DLC11-1-1-01	I	26.1	162	1,600	1,570	0.10	140	1.14	16.1	16.0	9.16	54.2	13.5	185	43.8	185	38.6
DLC11-1-1-02	I	22.8	255	1,590	1,410	0.41	663	4.11	49.7	36.2	16.5	81.3	15.5	133	34.7	134	26.9
DLC11-1-1-03	I	30.9	359	1,590	1,610	0.66	145	0.86	14.6	19.5	10.4	60.8	14.3	188	44.0	189	39.9
DLC11-1-1-04	I	37.6	33.7	1,610	1,900	0.11	181	1.13	18.8	21.7	12.5	69.9	17.0	220	51.8	220	45.0
DLC11-1-1-05	I	32.1	163	1,560	1,790	0.19	197	1.62	22.1	23.8	12.1	67.2	16.4	206	49.7	206	42.8
DLC11-1-1-06	I	21.4	0.00	1,560	1,700	0.11	150	0.94	16.6	19.5	10.9	63.4	15.2	198	47.7	199	41.4
DLC11-1-1-09	I	27.2	12.0	1,560	831	0.08	175	0.36	6.12	8.64	4.54	27.9	7.08	96.0	22.6	96	19.9
DLC11-1-1-10	I	31.6	0.00	1,530	718	0.09	186	0.53	7.28	9.01	4.58	26.8	6.41	73.7	18.2	73.7	15.5
DLC11-2-6	I	19.9	455	1,480	1,050	1.78	329	3.9	53.4	42.2	20.8	80.4	13.5	86.8	24.7	86.8	15.7
DLC11-2-8	I	28.9	230	1,450	1,120	1.09	490	7.66	88.4	63.9	30.7	110	16.9	87.7	26.9	87.7	14.5
DLC11-2-10	I	7.40	0.00	1,480	640	0.74	489	4.96	57.3	40.2	17.3	62.5	9.75	53.1	15.5	53.1	8.89
DLC11-2-12	I	0.00	0.00	1,450	1,460	0.34	453	3.52	50.2	47.9	25.5	103	17.6	113	33.1	113	19.8
MNP11-1-19-1	I	68.8	0.00	1,420	2,570	0.07	163	0.3	6.31	14.4	9.08	69.5	19.3	310	70.7	310	64.1
MNP11-1-19-5	I	45.5	100	1,420	3,270	0.19	315	0.86	15.4	28.0	14.8	114	30.2	384	94.5	384	72.1
MNP11-1-19-7	I	102	51.2	1,440	1,750	2.01	106	0.48	4.60	7.50	4.78	41.3	12.0	229	49.0	230	50.4
MNP11-1-19-8	I	88.7	0.00	1,450	2,250	0.53	106	0.18	3.34	6.80	5.01	41.9	13.4	283	60.8	284	60.4
LZ121-10	I	83.0	0.00	1,520	1,080	0.12	117	0.79	10.3	13.1	6.57	43.9	10.4	139	32.9	140	29.3
LZ121-12	I	86.6	0.00	1,490	1,380	0.04	280	0.74	11.8	16.3	8.55	56.4	13.9	178	42.7	178	37.2
DLS116-3	I	98.0	0.00	1,460	1,090	0.41	88.6	0.22	3.68	7.40	4.27	31.5	9.00	133	30.3	134	27.9
DLS116-4	I	83.6	249	1,460	2,670	0.59	150	0.36	3.96	11.6	9.17	68.3	24.9	443	102	444	92.6
DLS116-5	I	75.5	266	1,430	887	0.04	40.0	0.26	3.98	7.31	4.22	29.9	7.84	116	26.8	117	24.6
DLS116-6	I	237	0.00	1,420	1,010	0.54	62.8	0.29	2.18	3.50	2.63	20.5	6.43	129	27.6	130	29.6
DLS116-10	I	976	1,874	1,450	1,330	6.10	87.6	1.83	10.2	8.00	3.70	31.7	9.37	168	36.8	169	36.7
DLS116-12	I	211	300	1,430	1,850	0.60	76.1	0.31	4.26	9.18	5.01	49.2	14.4	235	53.7	236	47.1
DLS116-15	I	431	711	1,420	1,660	2.84	116	0.84	7.22	9.73	5.70	47.0	13.4	207	47.9	208	42.4
Average		115	209	1,490	1,540	0.79	212	1.53	19.5	19.7	10.3	58.1	13.9	184	43.5	184	37.7
MNP11-1-19-11	II	51.4	812	1,370	1,170	18.2	112	1.98	10.3	5.00	3.07	26.1	8.31	183	37.8	183	41.4
MNP11-1-19-12	II	48.3	518	1,380	1,330	43.4	135	3.08	10.7	6.26	4.01	29.8	9.67	202	41.9	202	45.6
MNP11-1-19-13	II	39.1	1,120	1,490	1,140	43.0	150	5.28	19.5	6.25	3.97	26.6	8.65	178	37.3	178	39.7
DLS116-9	II	37.0	292	1,410	1,010	48.2	307	7.87	36.7	16.0	8.22	38.1	9.50	103	25.3	104	21.1
DLS116-18	II	152	2,330	1,420	2,330	89.7	426	21.0	71.4	35.4	16.1	92.1	22.7	290	68.7	290	57.9
Average		65.6	1,020	1,420	1,400	48.5	226	7.84	29.7	13.8	7.07	42.5	11.8	191	42.2	191	41.1
LZ121-9	III	107	2,160	1,480	460	358	5,350	331	2,152	337	49.9	70.0	9.49	61.7	15.5	56.5	11.1
LZ121-21	III	726	1,400	1,370	2,650	706	7,110	328	1,357	243	92.0	213	33.1	237	56.3	216	43.4
LZ121-22	III	242	2,320	1,330	7,050	87.9	2,820	38.4	373	351	169	781	145	960	188	513	74.9
Average		358	1,960	1,400	3,390	384	5,100	232	1,294	310	104	355	62.5	420	86.6	262	43.1

values of 1.50 to 6.24‰, while the altered parts of type III zircons have even lower values (1.92–5.86‰). For both type II and III zircons, BSE-bright domains have higher $\delta^{18}O$ values than BSE-dark domains in the same crystal (Fig. 5; Table 2).

Geochemistry of nordmarkite, nordmarkite after fenitization, and nordmarkite after REE mineralization

The fresh, fenitized, and mineralized nordmarkites have progressively lower SiO_2 and $K_2O + N_2O$ contents (Fig. 12A-C; App. Table A3), and A/CNK values decrease from >0.7 to <0.5 (Fig. 12D). There also appears to be a trend of increasing CaO and K_2O and decreasing Na_2O with progressive alteration and mineralization.

Discussion

Zircon genesis

Hydrothermal alteration of zircon has been the subject of recent studies (Hoskin, 2005; Lichtervelde et al., 2009; Wang et al., 2014; Yang, W.B., et al., 2014) because of its significance to the understanding of mineralization processes in ore deposits, such as granite-related W-Sn, Cu, and REE deposits, skarn deposits (Yang, W.B., et al., 2014; Liu et al., 2015a, 2016; Zhao et al., 2016; Zeng et al., 2017), and porphyry Cu deposits (Lv et al., 2016; Banik et al., 2017). However, few studies have undertaken a detailed comparative investigation of the geochemistry and petrographic characteristics of fresh and altered zircon in relation to the origins and characteristics of ore-forming fluids related to REE mineralization.

Type I zircons are found in fresh nordmarkite, are transparent in transmitted light, and do not contain hydrothermal minerals. CL images show well-developed oscillatory zoning, and the zircons are homogeneous in BSE images. BSE and CL images and Raman spectra indicate that the zircon crystal structure has not been altered. In its ideal stoichiometry, zircon contains 32.8 wt % SiO_2 and 67.2 wt % ZrO_2. The unaltered type I zircons have near-stoichiometric compositions. For most samples, type I zircons have REE concentrations of 574 to 2,080 ppm (avg = 1,130 ppm), and Yb_N/Sm_N (1.66–71.9) and Th/U (0.03–0.56) ratios similar to those of magmatic and unaltered zircons in nepheline syenite pegmatites (Belousova et al., 2002, 2006). Therefore, we infer that type I zircons are primarily fresh and magmatic zircons. Type II zircons are found in nordmarkite adjacent to fenitization veins hosting arfvedsonite and aegirine-augite or fluorite-, barite- and quartz-bearing veins. In CL images, they

Table 3. *(Cont.)*

Yb	Lu	Hf	Ta	Pb	Th	U	LREE	HREE	ΣREE	L/H	Sm_N/La_N	Th/U	Yb_N/Sm_N	La_N/Yb_N	δEu	δCe
347	64.0	7,060	0.09	0.67	460	2,350	183	882	1,060	0.21	250	0.20	19.5	0.00	0.95	102
240	45.8	6,200	0.43	4.66	3,760	6,760	771	705	1,480	1.09	135	0.56	5.97	0.00	0.93	124
348	65.8	6,760	0.12	10.3	520	2,480	192	903	1,100	0.21	46	0.21	16.1	0.00	0.92	47.5
395	74.2	7,040	0.13	0.92	682	3,160	236	1,040	1,270	0.23	310	0.22	16.4	0.00	0.98	127
385	71.9	6,360	0.16	0.71	657	2,760	258	998	1,260	0.26	197	0.24	14.6	0.00	0.93	88.0
368	67.0	6,800	0.11	0.81	573	2,660	199	952	1,150	0.21	269	0.22	17	0.00	0.95	114
179	33.7	7,090	0.20	0.90	768	3,130	195	457	653	0.43	174	0.25	18.7	0.00	0.90	257
139	26.3	7,480	0.16	0.97	870	3,520	208	365	574	0.57	159	0.25	13.9	0.00	0.90	213
129	25.7	5,490	0.20	1.90	526	4,500	452	476	928	0.95	36.8	0.12	2.75	0.01	1.09	30.7
120	21.6	6,170	0.13	1.03	755	3,180	683	514	1,200	1.33	91.1	0.24	1.69	0.01	1.12	41.7
74.1	13.8	6,850	0.20	2.09	1,540	5,410	610	304	914	2.00	84.3	0.28	1.66	0.01	1.05	62.7
162	30.0	7,590	0.19	3.29	1,970	5,170	581	617	1,200	0.94	215	0.38	3.04	0.00	1.11	101
552	97.0	8,420	1.00	7.94	2,640	14,500	194	1,400	1,600	0.14	301	0.18	34.5	0.00	0.88	271
608	104	8,330	1.02	21.2	5,140	15,600	375	1,710	2,080	0.22	227	0.33	19.5	0.00	0.8	190
471	90.9	11,900	2.58	25.8	1,990	18,400	126	1,080	1,210	0.12	5.78	0.11	56.5	0.00	0.83	26.7
543	97.7	12,500	1.63	10.9	1,550	19,300	123	1,260	1,390	0.10	19.6	0.08	71.9	0.00	0.91	84.6
266	51.6	7,300	0.27	2.60	864	2,880	148	677	825	0.22	169	0.30	18.3	0.00	0.84	93.3
318	58.8	7,100	0.52	4.57	1,650	5,750	318	840	1,160	0.38	622	0.29	17.6	0.00	0.86	398
251	49.7	9,400	0.85	6.29	2,220	10,800	105	626	730	0.17	28.3	0.21	30.5	0.00	0.86	72.0
754	121	11,300	1.02	4.52	1,200	36,600	176	1,910	2,080	0.09	30.3	0.03	58.5	0.00	1.00	79.8
228	45.7	6,440	0.35	1.54	573	2,450	56.0	560	616	0.10	278	0.23	28.1	0.00	0.87	94.7
277	56.1	9,000	0.39	2.24	816	6,050	72.0	621	693	0.12	9.86	0.13	71.2	0.00	0.95	38.8
342	68.2	9,190	0.63	5.96	1,440	8,180	117	799	916	0.15	2.03	0.18	38.5	0.01	0.71	6.44
414	78.1	8,830	0.59	3.90	1,430	8,280	95.0	1,050	1,150	0.09	23.8	0.17	40.6	0.00	0.72	43.1
366	70.4	8,760	0.68	5.02	1,610	8,460	143	938	1,080	0.15	5.31	0.19	33.9	0.01	0.82	18.4
331	61.2	7,970	0.55	5.23	1,450	8,100	265	867	1,130	0.42	148	0.22	26.0	0.00	0.92	109
391	69.7	19,900	5.09	46.0	505	22,300	151	860	1,010	0.18	0.42	0.02	70.4	0.03	0.82	4.60
412	70.2	20,000	6.96	128	610	27,000	203	930	1,130	0.22	0.22	0.02	59.2	0.08	0.90	2.88
365	63.7	20,200	6.01	195	687	22,300	229	821	1,050	0.28	0.23	0.03	52.6	0.08	0.94	2.46
169	25.2	9,600	2.26	18.9	2,610	17,400	425	479	904	0.89	0.52	0.15	9.51	0.20	1.02	3.88
476	81.3	7,330	0.51	9.68	2,460	8,510	660	1,314	1,970	0.50	0.61	0.29	12.1	0.13	0.86	2.41
363	62.0	15,400	4.17	79.5	1,370	19,500	334	881	1,210	0.41	0.40	0.10	40.8	0.10	0.91	3.25
95.4	14.8	14,700	56.4	96.4	25,700	31,700	8,580	334	8,920	25.67	1.46	0.81	0.25	2.69	0.99	3.81
355	50.2	11,100	19.4	150	54,200	64,500	9,840	1,205	11,000	8.16	0.53	0.84	1.31	1.42	1.24	3.63
484	58.3	10,300	4.67	148	49,300	59,900	3,840	3,205	7,040	1.20	6.18	0.82	1.24	0.13	0.99	11.9
311	41.1	12,000	26.8	131	43,100	52,000	7,420	1,581	9,000	11.7	2.72	0.82	0.93	1.41	1.07	6.45

commonly show patchy or cloudy zoning, similar to other hydrothermal zircons (e.g., Pettke et al., 2005; Lichtervelde et al., 2009; Li et al., 2018). In BSE images, these zircons have irregular zoning, and the boundaries between bright and gray domains are irregular, with gray domains tending to occur along grain margins (i.e., likely fluid pathways). In some cases, due to the exsolution of hydrothermal fluids, amorphous domains at the edges of zircons are present. These observations indicate that type II zircons have experienced hydrothermal alteration, radiation damage, or a combination of both.

Based on electron microprobe analysis, type II zircons have lower and more variable SiO_2 and ZrO_2 contents (25.88–32.98 and 49.64–65.22 wt %, respectively) than type I zircons. Both type I zircons and the altered parts of type II zircons have similar chondrite-normalized REE patterns (Fig. 9). Type I zircons have light REE/heavy REE (LREE/HREE) ratios of 0.09 to 2.00 and La_N/Yb_N ratios less than 0.01. They display large and variable positive Ce anomalies with Ce/Ce* = 6.44 to 398 (Table 3). Altered regions of type II zircons have LREE/HREE ratios of 0.18 to 0.89 and La_N/Yb_N ratios of 0.03 to 0.20. They display large positive Ce anomalies with Ce/Ce* = 2.41 to 4.60 (Table 3).

Type III zircons are found in nordmarkite that is strongly affected by ore-forming fluids and hydrothermal alteration. They have a murky appearance under the microscope. In CL images, these zircons show convolute zoning, typical of hydrothermal zircons (Corfu et al., 2003). In BSE images, they show bright and gray regions with sharp contacts, and there are abundant thorite mineral inclusions in the gray domains. Similar observations have been documented for REE-rich apatite (e.g., Harlov et al., 2002; Li and Zhou, 2015). Amorphous domains are widespread in type III zircons due to the strong exsolution of ore-forming fluids, which is rare in type I but occasionally found in type II zircons. These textures are thought to reflect the hydrothermal alteration of zircons due to a dissolution-reprecipitation mechanism (Putnis et al., 2015).

Type III zircons have the lowest SiO_2 and ZrO_2 contents (23.59–32.80 and 37.38–64.71 wt %, respectively; App. Table A1). They have higher concentrations of UO_2, ThO_2, HfO_2, Ce_2O_3, and REOs than type I and II zircons. Type III zircons show both bright and gray regions in BSE images. In type III zircons, dark BSE domains have lower concentrations of UO_2, ThO_2, HfO_2, Ce_2O_3, and REOs than corresponding bright BSE domains, indicating that trace elements were leached from the zircon during hydrothermal alteration (App. Table A1; Fig. 13).

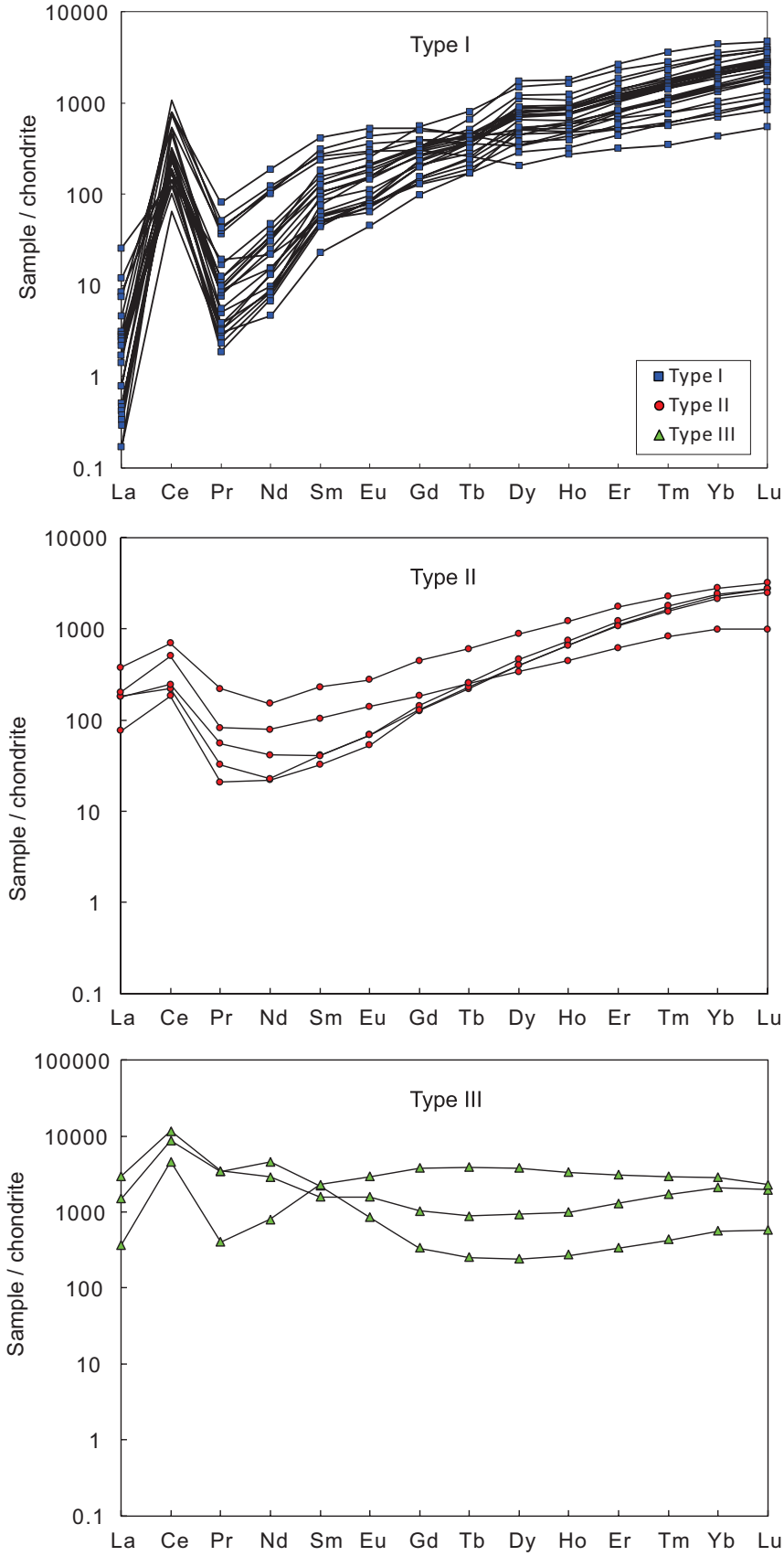

Fig. 9. Chondrite-normalized REE plots for type I, II, and III zircons from the Maoniuping, Lizhuang, and Dalucao deposits in the Mianning-Dechang REE belt.

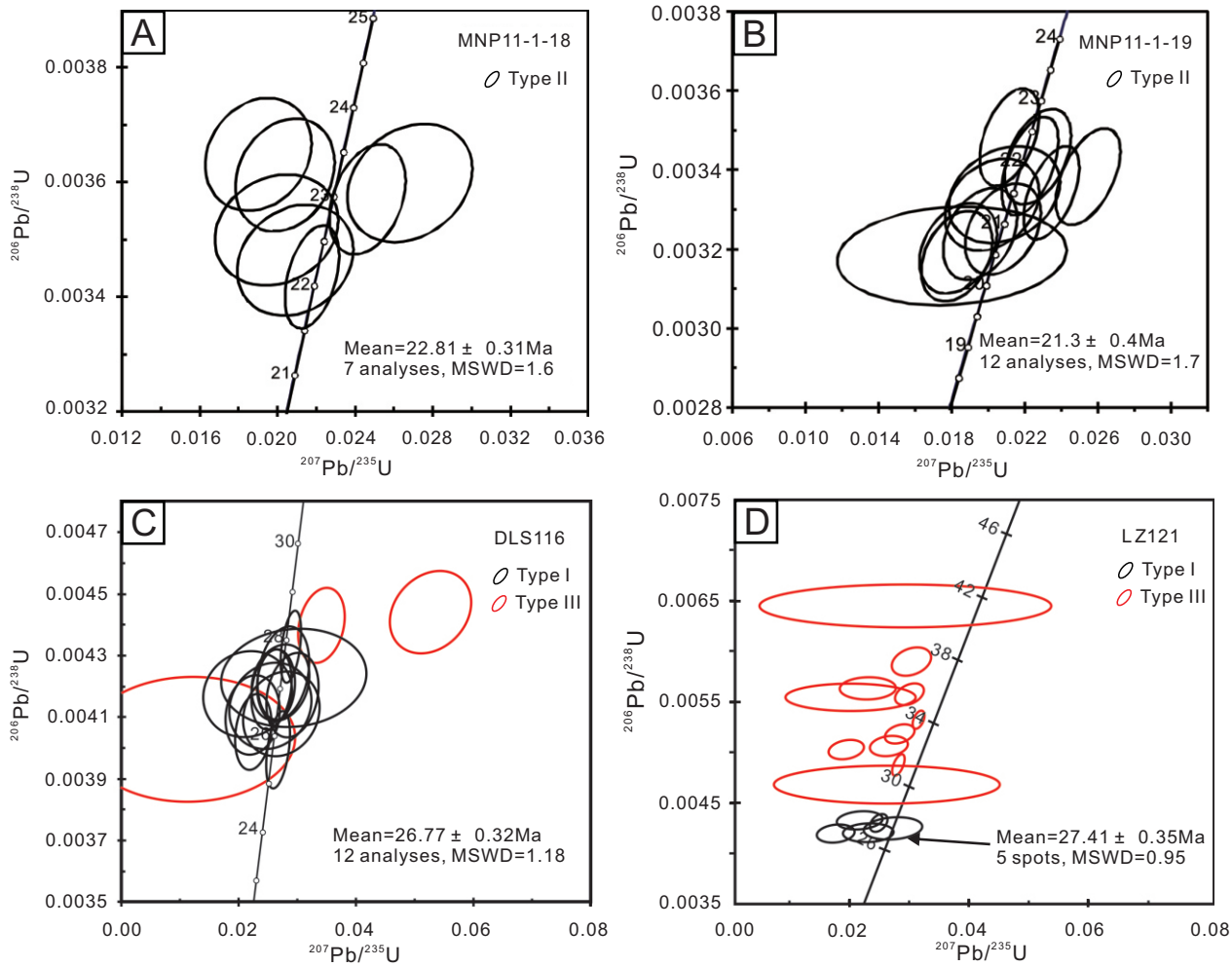

Fig. 10. SHRIMP zircon U-Pb ages for nordmarkites from (A, B) Maoniuping (type II), (C) Diaoloushan (types I, II), and (D) Lizhuang (types I, III) deposits. MSWD = mean standard of weighted deviates.

Type III domains have LREE/HREE ratios of 0.43 to 25.67 and La_N/Yb_N ratios of 0.07 to 2.69. They display large positive Ce anomalies with $Ce/Ce^* = 0.46$ to 11.9 (Fig. 9). In general, from type I to II to III zircons, REE concentrations increase from 1,130 to 1,210 to 9,000 ppm, respectively (Table 3). It appears that type III zircons interacted with ore-forming fluids with high REE concentrations. Our data show that the altered parts of type III zircons have higher concentrations of U, Th, Hf, Ce, and total REEs, and higher LREE/HREE ratios, than type I and II zircons (Fig. 9). Rubin et al. (1989) reported ThO_2 contents of up to 9.4 wt % in zircon from an alkaline rhyolite. Thus, zircons containing high contents of Th and U are not rare.

Although type II and III zircons have experienced both radiation damage and hydrothermal alteration, type III zircons interacted with highly evolved ore-forming fluids rather than hydrothermal fluids composed of magmatic and meteoric water. Type III zircons differ from the other zircons in that they contain abundant thorite mineral inclusions, along with minor barite and fluorite. This led to more extensive radiation damage induced by the thorite mineral inclusions with high U and Th concentrations (App. Fig. A1). This difference

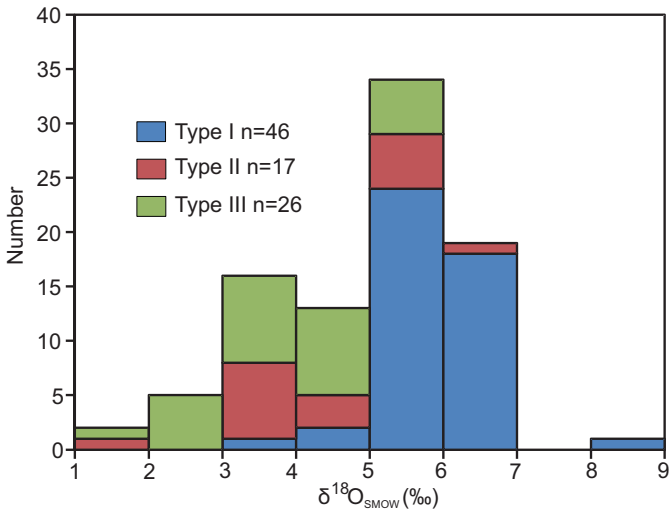

Fig. 11. Zircon $\delta^{18}O$ values for the Dalucao, Maoniuping, Lizhuang, and Muluozhai deposits in the Mianning-Dechang REE belt. SMOW = standard mean ocean water.

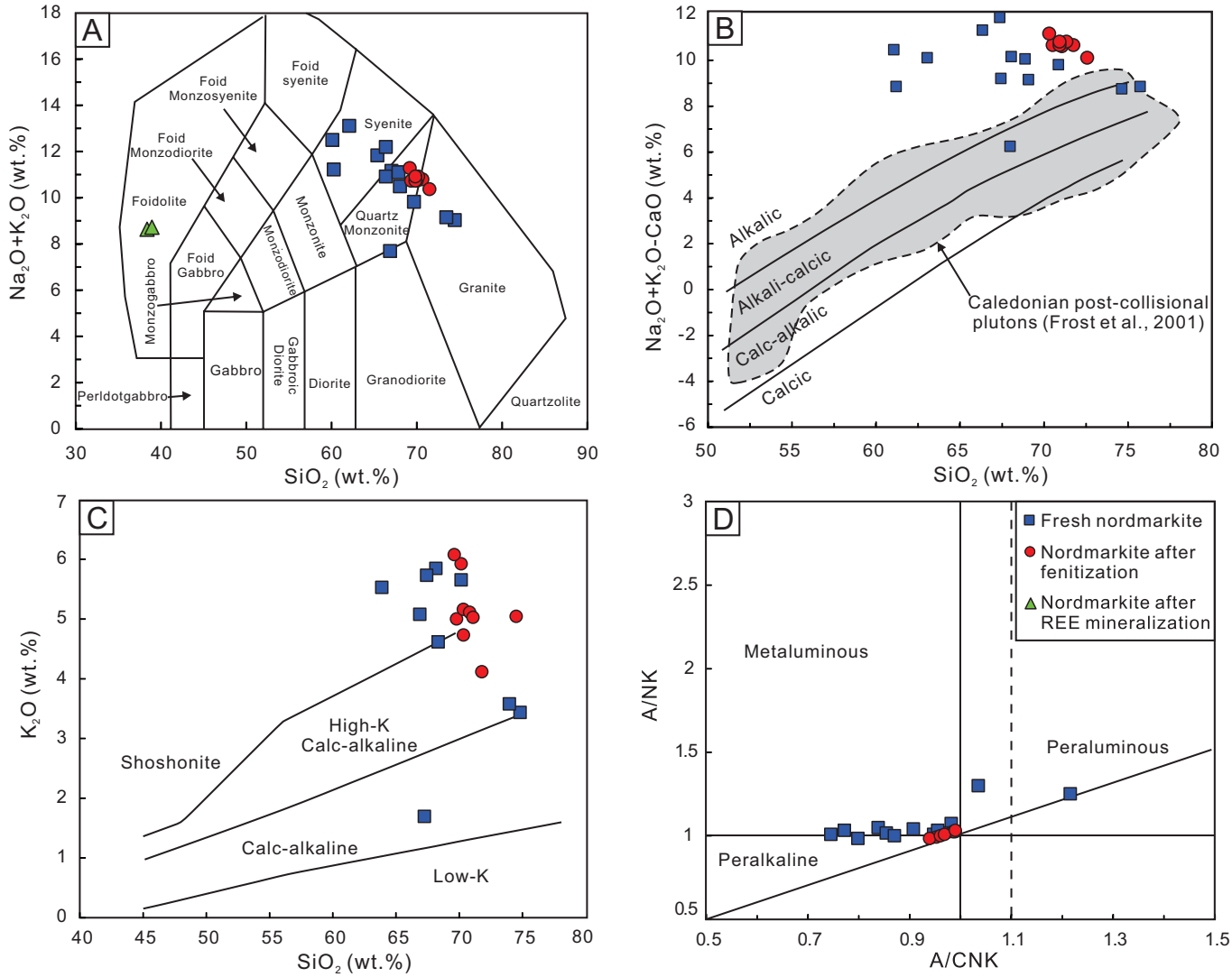

Fig. 12. Plots of (A) SiO_2 versus $Na_2O + K_2O$ (after Middlemost, 1994), (B) SiO_2 versus $Na_2O + K_2O + CaO$ (after Frost et al., 2001), (C) SiO_2 versus K_2O (after Peccerillo and Taylor, 1976), and (D) A/CNK versus A/NK for fresh nordmarkite, nordmarkite after fenitization, and nordmarkite after REE mineralization—which contain type I, II, and III zircons, respectively—in the Mianning-Dechang REE deposits.

between the type II and III zircons might reflect three factors. Firstly, the Lizhuang carbonatite-nordmarkite complex (containing type III zircons) is more Th rich (46–294 ppm) than the complexes at Maoniuping (1–60 ppm) and Dalucao (5.4–49.5 ppm) and might therefore have acted as a source of Th for the formation of thorite inclusions. Secondly, the presence of Th-rich bastnäsite (1,179–1,394 ppm) suggests that the Lizhuang ore-forming fluids were rich in Th and might have acted as a source of Th for the thorite inclusions (Guo and Liu, 2019). Thirdly, nordmarkite with type III zircons interacted with highly evolved ore-forming fluids rather than the hydrothermal fluids that affected the type II zircons.

Similarities in the geochemical signatures and morphologies of type I, II, and III zircons from these various occurrences of nordmarkite indicate that these zircons share the same origin (Figs. 4–9). With increasing LREE contents from type I to III zircons, the data for type II and III zircons fall into the field of hydrothermal zircons (Fig. 14). This suggests that both type II and III zircons were overprinted by later fluids, unlike the unaltered magmatic type I zircons.

Alteration-induced U-Th-Pb isotope changes

Most type II zircons and zircon domains have U and Th contents of >8,510 ppm and up to 2,610 ppm. In addition, most type III zircons and zircon domains have U concentrations of >31,700 ppm and high Th contents of up to 54,200 ppm (App. Table A4), which are higher than most magmatic zircons (U = 100–500 ppm; Marsellos and Garver, 2010). The radiation damage associated with the high U and Th concentrations gives the zircons a darker appearance under an optical microscope (Fig. 4D).

Given a similar thermal history, zircons with higher U and Th show more radiation damage than those with lower U and Th concentrations (Marsellos and Garver, 2010). It has

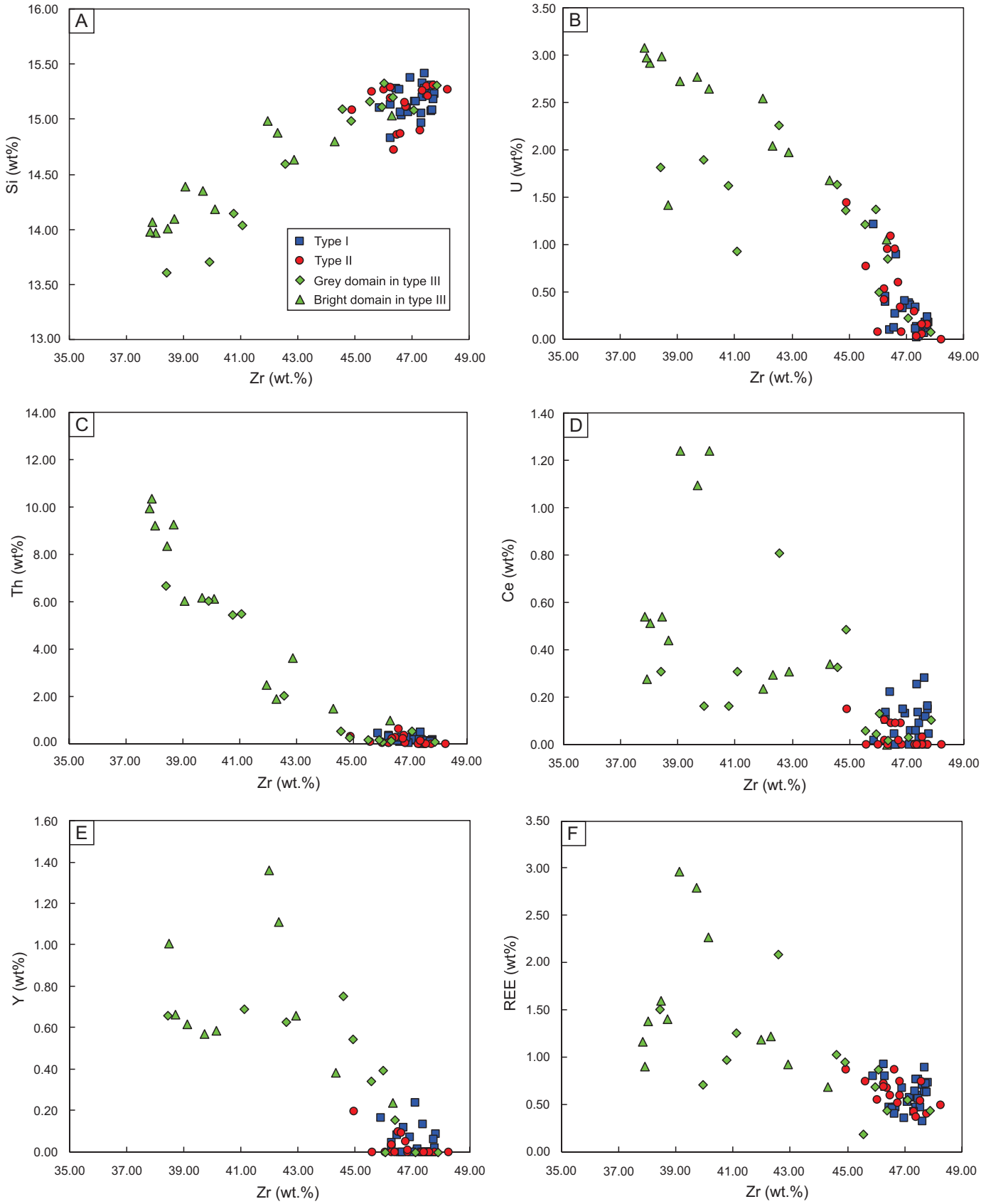

Fig. 13. Plots of (A) Si versus Zr, (B) U versus Zr, (C) Th versus Zr, (D) Ce versus Zr, (E) Y versus Zr, and (F) REE versus Zr for the three types of zircon from the Mianning-Dechang REE deposits.

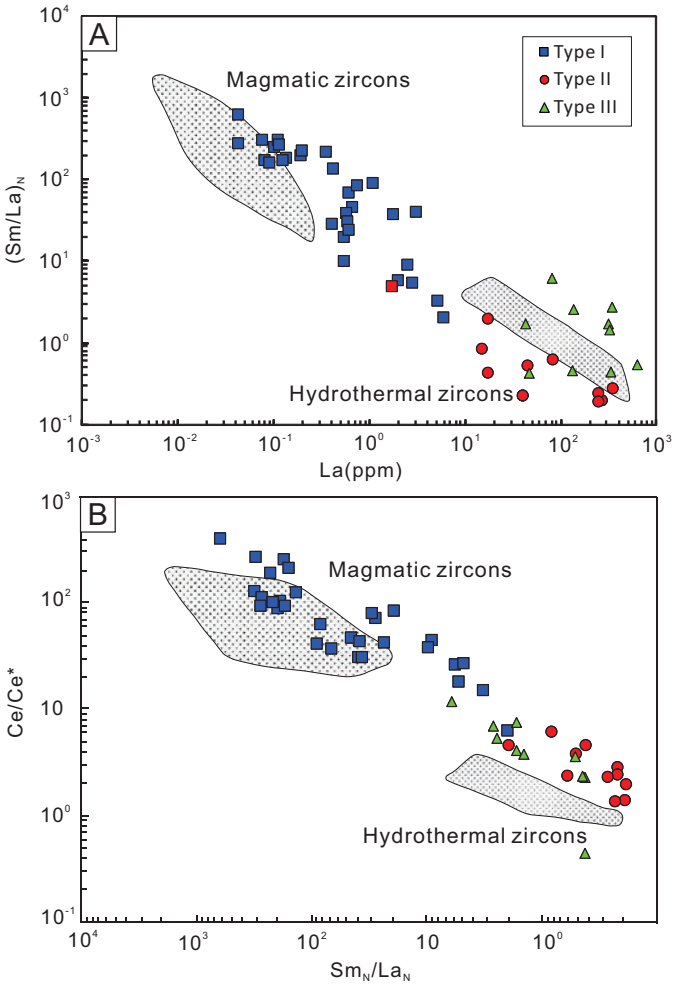

Fig. 14. (A, B) Discrimination diagrams for type I, II, and III zircons. Data for type I zircons all plot in the unmodified (magmatic) zircon field, whereas those for type II and III zircons plot close to the hydrothermal zircon field. The discrimination diagrams are modified from Hoskin (2005).

been shown that α-recoil is mainly responsible for the radiation damage of zircon (e.g., Ewing et al., 2003; Nasdala et al., 2004; Marsellos and Garver, 2010), and the alpha dose (α-decay events/mg) can be calculated (assuming no annealing) as follows (Nasdala et al., 2001; Palenik et al., 2003):

$$D_\alpha^T = 8N_1[\exp(\lambda_1 t) - 1] + 7N_2[\exp(\lambda_2 t) - 1] + 6N_3[\exp(\lambda_3 t) - 1], \quad (1)$$

where D_α^T is the total dose in α-decay events/mg; N_1, N_2, and N_3 are the present numbers of ^{238}U, ^{235}U, and ^{232}Th atoms, respectively, in atoms/mg; λ_1, λ_2, and λ_3 are the decay constants for ^{238}U, ^{235}U, and ^{232}Th, respectively, in yr^{-1}; and t is the age of the zircon.

Type II and III zircons have $D_\alpha^T = 6$ to 400×10^{16} α-decay events/mg and 75% show $D_\alpha^T > 100 \times 10^{15}$ α-decay events/mg (App. Table A4), corresponding to a moderate to high degree of radiation damage in zircon (Murakami et al., 1991), if not annealed. In contrast, most type I zircons have $D_\alpha^T < 8 \times 10^{16}$ α-decay events/mg (App. Table A4), with a correspondingly low degree of radiation damage. From type I to II to III zircons, D_α^T values increase gradually, suggesting a concomitant increase in radiation damage (Nasdala et al., 2001, 2008; Ewing et al., 2003; Marsellos and Garver, 2010), in accordance with the results from our Raman study.

Raman spectroscopy is a powerful tool in the analysis of short- and medium-range structural variations and in examining the relationship between radiation damage in zircon and Raman spectra (e.g., Nasdala et al., 2001, 2008; Ewing et al., 2003; Marsellos and Garver, 2010). Altered zircons have a lower Raman intensity but higher full width at half maxima (FWHM) than fresh zircons (Fig. 8D). Fresh magmatic zircons from all the deposits show strong Raman intensity and small wave number shifts, indicating that their structures have not changed (Fig. 8A). In contrast, type II and III zircons have lower ZrO_2 and SiO_2 contents (App. Table A1), indicating a significant loss of Zr. They also contain nonstoichiometric elements (U, Hf, Th, and LREEs) in higher concentrations than in magmatic zircon (Fig. 13). This is consistent with the incompatibility of larger-radii LREEs and their absence in the primary magmatic zircons of type I (Hanchar and Van Westrenen, 2007). The deviation of type III zircons from the radiation damage trend (RDT) (Geisler et al., 2001a) indicates that both radiation damage and ore-forming fluids contribute to the alteration of these zircons.

Radiation damage of type I zircons is limited, and most type I zircons have low D_α^T of 0.6 to 29.5 α-decay events/mg, with an average of 12.7 α-decay events/mg. Thus, U-Pb dates of type I zircons could represent the formation age of the carbonatite-nordmarkite complexes, as they are fresh and unaltered.

Experimental results indicate that alteration of zircon is common in alkali- or Ca-bearing fluids, and the altered domains show strong enrichment in Th and Si, coupled with strong depletion in U, Pb, and Y + REEs (Harlov et al., 2012). Disturbance or resetting of the U-Pb system means that dating of these altered zircons or zircon domains is unlikely to constrain the timing of magmatism. However, despite the loss of Si and Zr (Fig. 13) and increase in U, Th, and other elements, type III zircons have retained REE patterns and isotopic systematics similar to those of type I and type II zircons. In high-Th-U zircon that shows structural radiation damage, the textures are the result of a diffusion reaction process in which a hydrous species diffuses inward and catalyzes structural recovery. Nanoscale pores develop, soluble elements such as Ca, Al, and Fe are added, and radiogenic Pb is lost (Geisler et al., 2007). In both aqueous fluids, replacement of zircon with an undamaged structure by a coupled dissolution-reprecipitation process can produce similar textures. The reacted domains typically have lower trace element contents and can contain micron-sized pores and inclusions of U-, Th-, or Y-bearing phases (Geisler et al., 2007). The diffusion-reaction process can retain some memory of the parental isotopic compositions, whereas the coupled dissolution-reprecipitation process results in complete reequilibration of the parental isotopic systems (Geisler et al., 2007). Thus, U-Pb dates for the type II zircons are slightly younger than those of the primary type I zircons (Ling et al., 2016; Figs. 10, 15), likely due to Pb loss from altered domains that experienced radiation damage.

Type III zircons in the Lizhuang deposit have the highest U (8,510–27,000 ppm) and Th (25,700–54,200 ppm) contents among the three types of zircon. Their corresponding D_α^T values are 64 to 687 α-decay events/mg, with an average

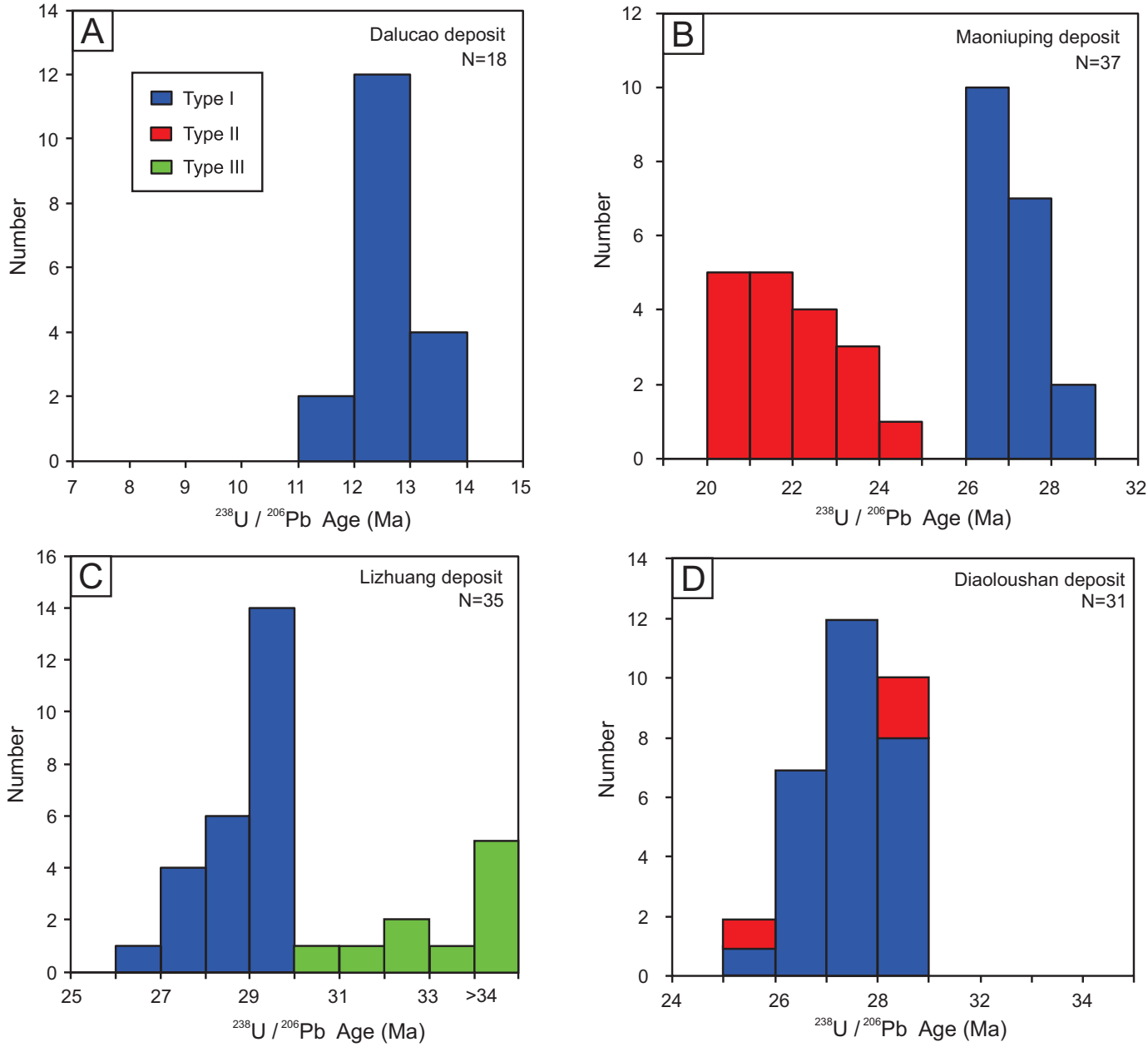

Fig. 15. Histograms of SHRIMP U-Pb zircon ages for nordmarkites from (A) Dalucao (type I zircons), (B) Maoniuping (types I and II zircons), (C) Lizhuang (types I and III zircons), and (D) Diaoloushan (types I and II zircons) deposits.

of 144 α-decay events/mg. These zircons experienced significant radiation damage. Based on the petrographic characteristics and Raman spectra of type III zircons, the crystal lattice has been strongly damaged by U-Th decay, and structural changes have resulted from thermal annealing. In addition, numerous small-sized thorite mineral inclusions are present (Figs. 5–7). The type III zircons exhibit an obvious high-U effect in that the apparent U-Pb ages show a positive correlation with U contents (App. Table A2; Fig. 15) as described by Li (2016). This effect could be caused by the mixture of crystalline and amorphous regions of the radiation-damaged zircons, as radiogenic Pb favors the amorphous SiO_2, whereas U favors the ZrO_2 lattice, resulting in ionization efficiency differences between Pb and U during analysis (Yang, Y.H., et al., 2014).

Dating of unaltered zircons (type I) and bastnäsite might yield robust U-Pb and Th-Pb ages of these REE deposits. We propose that other minerals, such as monazite, xenotime, bastnäsite, and titanite, might also be suitable for dating (Li, 2016).

Metasomatizing fluid and REE mineralization stages

Previous studies have proposed that mixing of magmatic fluids, meteoric fluids, and CO_2 derived from the decarbonation of carbonatite was responsible for the composition of the ore-forming fluids (App. Fig. A2) (Liu et al., 2015b; Liu and Hou, 2017). The proportion of these components in the

ore-forming fluids might have changed during fluid evolution, leading to the stronger modification of the type III zircons.

Given that type II and III zircons interacted with evolved metasomatizing fluids with geochemical characteristics different from the REE ore-forming fluids, three stages of REE mineralization can be recognized. In the first stage, the carbonatite-nordmarkite complexes and type I zircons formed without being affected by fluids and experienced limited REE mineralization (Fig. 16A). As the fluids evolved, the wall-rock nordmarkites were fenitized to an assemblage of arfvedsonite, aegirine-augite, and phlogopite. In this stage, the fluids still had the capacity to transport REEs, and, consequently, no major REE mineralization developed. The earliest minerals to precipitate in the veins were K-Na silicates, such as aegirine-augite and arfvedsonite, at temperatures of 350° to 480°C (Shu and Liu, 2019). This caused progressive enrichment in Na, K, Ca, Mg, F, Cl, CO_2, and SO_4 (Fig. 16B) (Liu et al., 2019). In this stage, type II zircons interacted with these alkali-rich fluids (Fig. 16B), which facilitated zircon alteration (Ayers et al., 2012; Harlov et al., 2012; Li et al., 2018).

As the evolved fluids cooled, they reached the solubility limits for CaF_2, $BaSO_4$, and $CaCO_3$, triggering the deposition of fluorite, barite, and calcite in fractures that had not yet been blocked by earlier crystallized material. Voluminous deposition of fluorite and calcite, and also of barite, further raised the fluid concentrations of LREEs, while simultaneously removing complexing ligands (F^-, SO_4^{2-}, Cl^-, and CO_3^{2-}) from the fluid. The loss of these anions and decreasing temperature severely diminished the REE-transporting capacity of the fluid, triggering bastnäsite precipitation at a large scale (stage III) at temperatures of 160° to 240°C (Guo and Liu, 2019) (Fig. 16C). In this stage, Na, K, Ca, Mg, F, Cl, CO_2, and SO_4 fluid concentrations reached their highest values, and the pH increased (Zheng and Liu, 2019). More importantly, the geochemistry of the bastnäsite implies that the fluids had high contents of U, Th, Pb, Zr, and Hf (Guo and Liu, 2019), which in turn implies that highly evolved ore-forming fluids were also rich in these elements.

Zirconium is generally assumed to be insoluble in aqueous fluids (Pearce and Cann, 1973); however, recent research indicates that Zr is mobile in F-rich fluids (Rubin et al., 1993; Aja et al., 1995, 1997; Bau and Dulski, 1995; Veksler et al., 2005; Ayers et al., 2012; Li et al., 2018). Thus, type III zircons experienced more alteration than type II zircons, given the evolved ore-forming fluids had higher pH values and contents of F^- and other alkali ions. Recent experimental studies have shown that zircon is more readily altered in alkaline, rather than acidic, fluids (Harlov et al., 2012). This suggests that the metasomatic fluids that altered the zircon were at most moderately acidic.

The altered domains of the zircons have lower $\delta^{18}O$ values than the unaltered domains (Figs. 5, 11), indicating that the metasomatic fluids were isotopically light. Meteoric water is typically isotopically light, and fluid inclusion and stable isotopic data indicate that meteoric water was involved in the ore-forming fluids (Liu et al., 2015b; Liu and Hou, 2017). We therefore suggest that meteoric water was a component in the metasomatic fluids and facilitated the fluid cooling and REE mineralization (Liu et al., 2019). Tracing the evolution of the ore-forming fluids from the REE deposits is challenging but

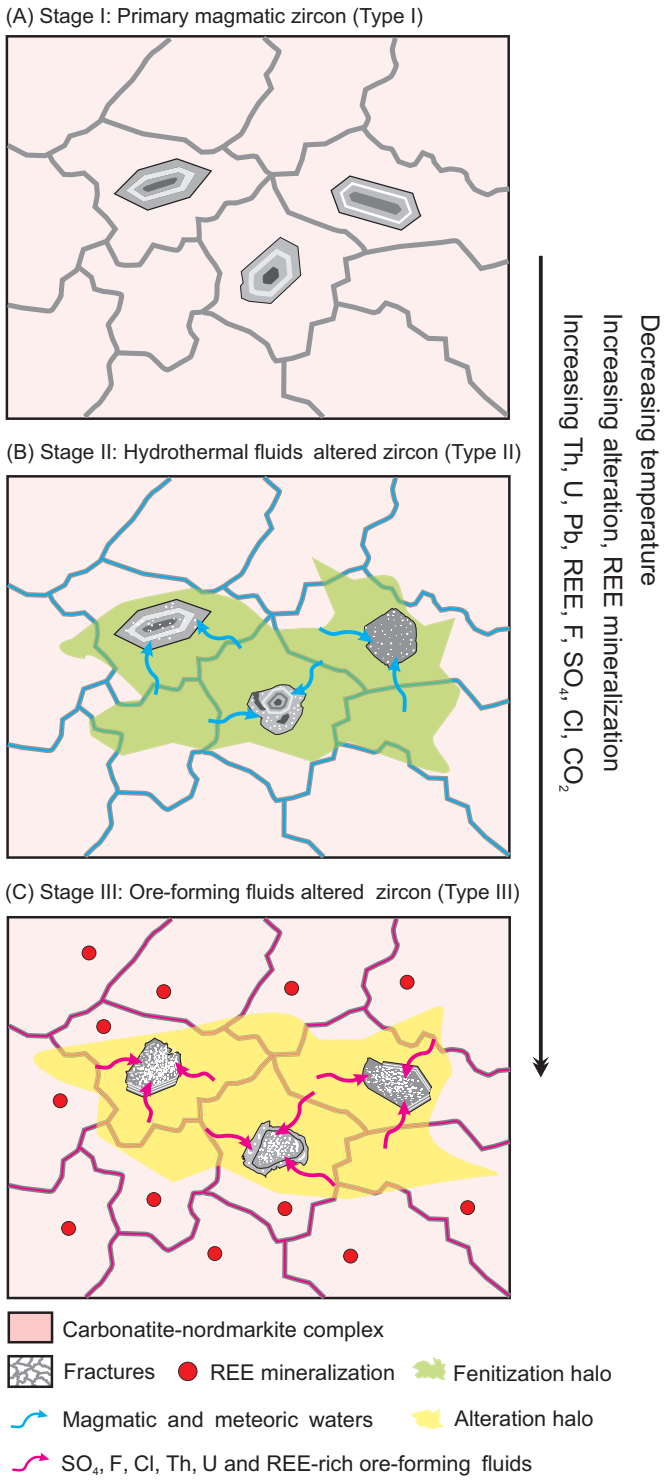

Fig. 16. Schematic model of the formation of type I, II, and III zircons and REE mineralization stages in the Mianning-Dechang REE deposits. (A) In the fresh carbonatite-nordmarkite complex (stage I), type I zircons are fresh and unaltered. (B) In the fenitized carbonatite-nordmarkite complex (stage II), type II zircons were altered by fluids composed of magmatic and meteoric waters, which were rich in Na, K, Cl, F, CO_2, and Ba but undersaturated with REEs. (C) In the REE-mineralized and altered carbonatite-nordmarkite complex (stage III), type III zircons interacted with highly evolved ore-forming fluids with high contents of Na, K, F, Cl, SO_4^{2-}, U, Th, Hf, and Ce. From stages I to III, the Th, U, Pb, REE, F, Cl, SO_4^{2-}, and Hf contents of ore-forming fluids increased and the ore-forming fluid temperatures decreased.

appears to be possible from the various types of zircon in the nordmarkites. Mineral REE, U, and Th contents and Th/U ratios increase with decreasing $\delta^{18}O$ values (8.6–1.4‰) (Fig. 17), Raman spectral shift, and broadening as indicated by the chemical compositions of zircon (Fig. 8). Thus, petrographic studies, oxygen isotope data, micro-Raman spectroscopy, and geochemical characteristics of zircons are effective tools for evaluating zircon alteration. More importantly, the geochemical and petrographic data for the various types of zircon suggest that nordmarkite was also the main source of REEs for the deposit and that the zircons record the formation process of the deposit.

We classified the zircons from the nordmarkites into three types, based on the degree of alteration and occurrence. These three types of zircon also correspond to the three main stages of REE mineralization. These geochemical and petrographic characteristics might also be utilized as a guide for REE mineralization and exploration. We present a model for the relationship between the zircons and carbonatite-nordmarkite complexes in Figure 16.

In global examples of carbonatite-related REE deposits, such as Bayan Obo (Song et al., 2018), Mountain Pass (Castor, 2008), and Maoniuping (Liu et al., 2019), the carbonatites have been assumed to be the main REE source. However, the present study has identified distinct signatures in zircon that reflect stages of alteration with respect to the formation of REE deposits. Type III zircons suggest that a highly evolved ore-forming fluid existed that was rich in F, Ba, SO_4, REEs, Ca, and Th, which might have also facilitated the REE transport and mineralization. Our results suggest that nordmarkite, rather than carbonatite alone, could be a significant contributor as the REE source, particularly given that 80% of carbonatites worldwide are associated with silicate rocks (Woolley and Kjarsgaard, 2008). Further investigation into the mineralization role of silicate magmas in other carbonatite-related deposits is required.

Conclusions

Our study leads to the following main conclusions regarding zircon alteration in the carbonatite-nordmarkite complexes in the Mianning-Dechang REE belt, as well as some broader implications.

1. The zircons in the nordmarkites can be classified into three general types, which represent three main stages of REE mineralization. Primary magmatic type I zircons occur in unaltered nordmarkite; type II zircons are present in nordmarkite that experienced fenitization by hydrothermal

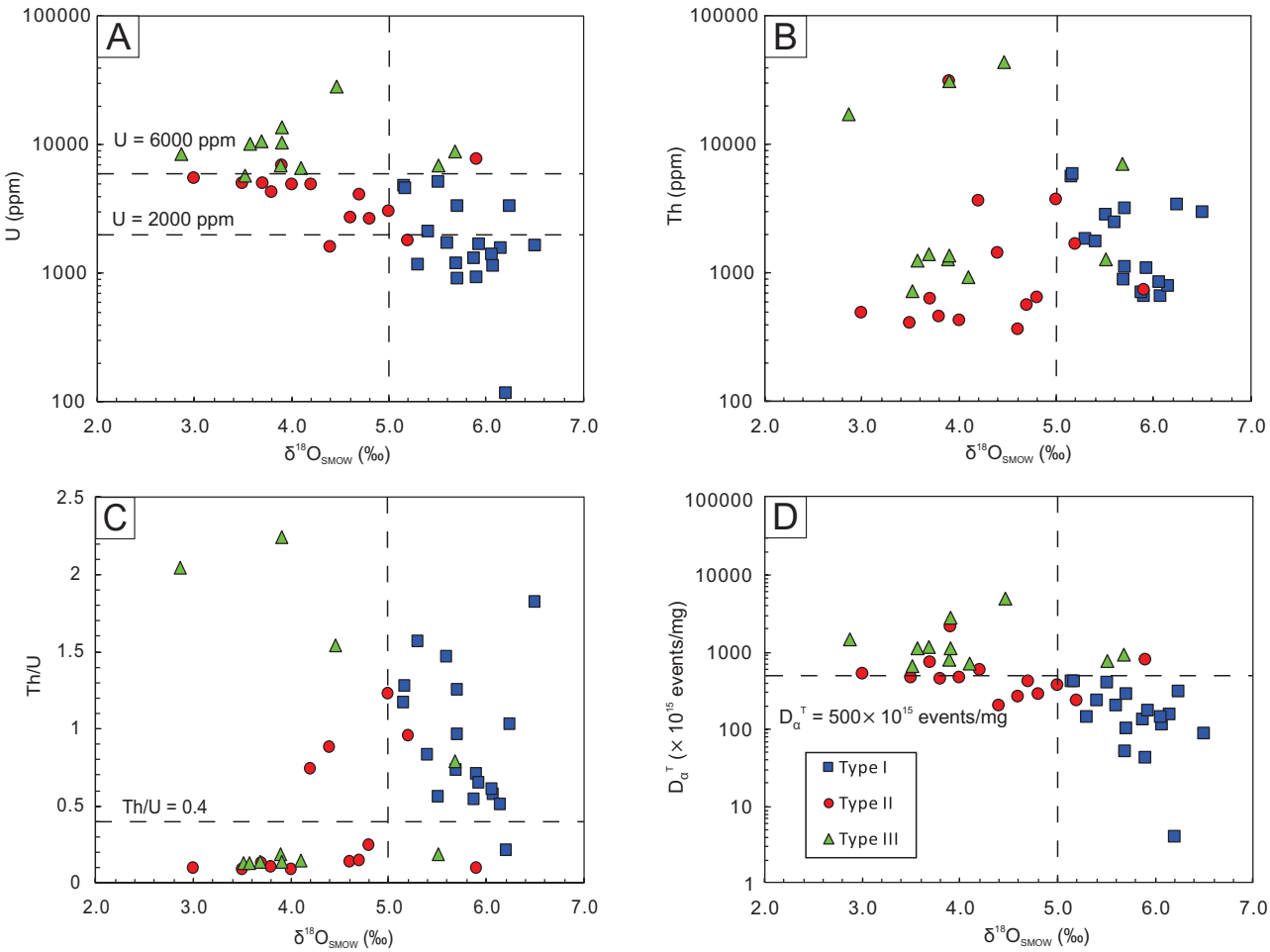

Fig. 17. Plots of (A) U versus $\delta^{18}O$, (B) Th versus $\delta^{18}O$, (C) Th/U versus $\delta^{18}O$, and (D) D_α^T versus $\delta^{18}O$ for type I, II, and III zircons from the Mianning-Dechang REE deposits. SMOW = standard mean ocean water.

fluids; type III zircons are present in nordmarkite that interacted with ore-forming fluids, and these zircons have undergone extensive alteration and radiation damage and contain abundant thorite and minor fluorite, celestite, and barite inclusions. From type I to III zircons, REE contents and radiation damage progressively increase due to the influx of REE, U, and Th from hydrothermal and ore-forming fluids. Type II and III zircons are not suitable for U-Pb dating.

2. Based on petrographic observations and geochemical compositions of the zircons, a highly evolved ore-forming fluid rich in F, Cl, SO_4, U, Th, Hf, and REEs facilitated REE mineralization. Influx of meteoric water into the ore-forming fluids led to low $\delta^{18}O$ values in both type II and III zircons and caused the precipitation of REEs.
3. Petrographic observations, BSE and CL images, Raman spectra, major and trace element data, and oxygen isotope data enable evaluation of the degree of alteration and radiation damage of zircons. This approach, applied to various types of zircon, might provide clues to REE mineralization processes. For REE mineralization in carbonatite-nordmarkite systems and possibly other magmatic deposits, the occurrence of type III zircons might be indicative of the presence of economic REE deposits.

Acknowledgments

This study was financed by the Strategic Priority Research Program of the Chinese Academy of Sciences (grant XDA20070304), the National Key Research and Development Project of China (2016YFC0600310), the National Natural Science Foundation of China (41772044), the CAS Hundred Talents Project to Jian-Feng Gao, the IGCP/SIDA (600) project, Fundamental Research Funds for the Chinese Academy of Geological Sciences (YYWF201705), and the Geological Survey Program of the China Geological Survey, Ministry of Natural Resources (DD20190060). We thank journal editor Larry Meinert, associate editor Massimo Chiaradia, an anonymous reviewer, and Dr. Li Xiaochun and Wan Yusheng for their encouragement and helpful suggestions.

REFERENCES

Aja, S.U., Wood, S.A., and Williams-Jones, A.E., 1995, The aqueous geochemistry of Zr and the solubility of some Zr-bearing minerals: Applied Geochemistry, v. 10, no. 6, p. 603–620.

——1997, The solubility of some alkali-bearing Zr minerals in hydrothermal solutions: Materials Research Society, Online Symposium Proceedings, v. 432, p. 69–74.

Ayers, J.C., Zhang, L., Luo, Y., and Peters, T., 2012, Zircon solubility in alkaline aqueous fluids at upper crustal conditions: Geochimica et Cosmochimica Acta, v. 96, p. 18–28.

Banik, T.J., Coble, M.A., and Miller, C.F., 2017, Porphyry Cu formation in the middle Jurassic Yerington batholith, Nevada, USA: Constraints from laser Raman, trace element, U-Pb age, and oxygen isotope analyses of zircon: Geosphere, v. 13, no. 4, doi:10.1130/GES01351.1.

Bau, M., and Dulski, P., 1995, Comparative study of yttrium and rare-earth element behaviors in fluorine-rich hydrothermal fluids: Contributions to Mineralogy and Petrology, v. 119, p. 213–223.

Belousova, E.A., Walters, S., Griffin, W.L., O'Reilly, S.Y., and Fisher, N.I., 2002, Zircon trace-element compositions as indicators of source rock type: Contributions to Mineralogy and Petrology, v. 143, p. 602–622.

Belousova, E.A., Griffin, W.L., and O'Reilly, S.Y., 2006, Zircon crystal morphology, trace element signatures and Hf isotope composition as a tool for petrogenetic modelling: Examples from eastern Australian granitoids: Journal of Petrology, v. 47, p. 329–353.

Black, L.P., Kamo, S.L., Williams, I.S., Mundil, R., Davis, D.W., Korsch, R.J., and Foudoulis, C., 2003, The application of SHRIMP to Phanerozoic geochronology; a critical appraisal of four zircon standards: Chemical Geology, v. 200, p. 171–188.

Black, L.P., Kamo, S.L., Allen, C.M., Davis, D.W., Aleinikoff, J.N., Valley, J.W., Mundil, R., Campbell, I.H., Korsch, R.J., Williams, I.S., and Foudoulis, C., 2004, Improved Pb-206/U-258 microprobe geochronology by the monitoring of a trace-element-related matrix effect; SHRIMP, ID-TIMS, ELA-ICP-MS and oxygen isotope documentation for a series of zircon standards: Chemical Geology, v. 205, p. 115–140.

Bouvier, A.-S., Ushikubo, T., Kita, N.T., Cavosie, A.J., Kozdon, R., and Valley, J.W., 2012, Li isotopes and trace elements as a petrogenetic tracer in zircon: Insights from Archean TTGs and sanukitoids: Contributions to Mineralogy and Petrology, v. 163, p. 745–768.

Castor, S.B., 2008, The Mountain Pass rare-earth carbonatite and associated ultrapotassic rocks, California: The Canadian Mineralogist, v. 46, p. 779–806.

Cavosie, A.J., Valley, J.W., and Wilde, S., 2007, The oldest terrestrial mineral record: A review of 4400 to 4000 Ma detrital zircons from Jack Hills, Western Australia: Developments in Precambrian Geology, v. 15, p. 91–111.

Compston, W., 1992, Zircon U-Pb ages for the early Cambrian time-scale: Journal of the Geological Society, London, v. 149, p. 171–184.

Corfu, F., Hanchar, J.M., Hoskin, P.W.O., and Kinny, P., 2003, Atlas of zircon textures: Reviews in Mineralogy and Geochemistry, v. 53, p. 469–500.

Ewing, R.C., Meldrum, A., Wang, L., Weber, W.J., and Corrales, L.R., 2003, Radiation effects in zircon: Reviews in Mineralogy and Geochemistry, v. 53, p. 378–420.

Frost, B.R., Arculus, R.J., Barnes, C.G., Collins, W.J., Ellis, D.J., and Frost, C.D., 2001, A geochemical classification of granitic rock suites: Journal of Petrology, v. 42, p. 2033–2048.

Gao, S., Liu, X.M., Yuan, H.L., Hattendorf, B., Günther, D., Chen, L., and Hu, S.D., 2002, Analysis of forty-two major and trace elements in USGS and NIST SRM glasses by LA-ICPMS: Geostandards and Geoanalytical Research, v. 26, no. 2, p. 181–196.

Geisler, T., Pidgeon, R.T., Bronswijk, W.V., and Pleysier, R., 2001a, Kinetics of thermal recovery and recrystallization of partially metamict zircon: A Raman spectroscopic study: European Journal of Mineralogy, v. 13, p. 1163–1176.

Geisler, T., Ulonska, M., Schleicher, H., Pidgeon, R.T., and Bronswijk, W.V., 2001b, Leaching and differential recrystallization of metamict zircon under experimental hydrothermal conditions: Contributions to Mineralogy and Petrology, v. 141, p. 53–65.

Geisler, T., Schaltegger, U., and Tomaschek, F., 2007, Re-equilibration of zircon in aqueous fluids and melts: Elements, v. 3, p. 43–50.

Guo, D.X., and Liu, Y., 2019, Occurrence and geochemistry of bastnäsite in carbonatite-related REE deposits, Mianning-Dechang REE belt, Sichuan Province, SW China: Ore Geology Reviews, v. 107, p. 266–282.

Guo, Z.F., Hertogen, J., Liu, J.Q., Pasteels, P., Boven, A., Punzalan, L., He, H.Y., Luo, X.J., and Zhang, W.H., 2005, Potassic magmatism in western Sichuan and Yunnan Provinces, SE Tibet, China: Petrological and geochemical constraints on petrogenesis: Journal of Petrology, v. 46, p. 33–78.

Guo, D.X., Liu, Y., Chen, C., Jiang, H., Li, Z.J., Li, D.L., and Ma, W., 2017, Mineral characteristics of zircons in the syenite-carbonatite complex in the Mianning-Dechang REE ore belt, Sichuan Province, SW China: Indicative of REE mineralization: Acta Petrologica et Mineralogica, v. 36, p. 343–59 (in Chinese with English abs.).

Hanchar, J.M., and Van Westrenen, W., 2007, Rare earth element behavior in zircon-melt systems: Elements, v. 3, p. 37–42.

Harley, S.L., and Kelly, N.M., 2007, Zircon tiny but timely: Elements, v. 3, p. 13–18.

Harley, S.L., Kelly, N.M., and Moller, A., 2007, Zircon behavior and the thermal histories of mountain chains: Elements, v. 3, p. 25–30.

Harlov, D., Lewerentz, A., and Schersten, A., 2012, Alteration of zircon in alkaline fluids: Nature and experiment: Mineralogical Magazine: Goldschmidt Conference Abstracts, v. 76, no. 6, p. 1813.

Harlov, D.E., Andersson, U.B., Förster, H.J., Nyström, J.O., Dulski, P., and Broman, C., 2002, Apatite-monazite relations in the Kiirunavaara magnetite-apatite ore, northern Sweden: Chemical Geology, v. 191, p. 47–72.

Harrison, T.M., 2009, The Hadean crust: Evidence from N4 Ga zircons: Annual Review of Earth and Planetary Sciences, v. 37, p. 479–505.

Hoskin, P.W.O., 2005, Trace-element composition of hydrothermal zircon and the alteration of Hadean zircon from the Jack Hills, Australia: Geochimica et Cosmochimica Acta, v. 69, p. 637–648.

Hou, Z.Q., and Zhang, H.R., 2015, Geodynamics and metallogeny of the eastern Tethyan metallogenic domain: Ore Geology Reviews, v. 70, p. 346–384.
Hou, Z.Q., Tian, S.H., Yuan, Z.X., Xie, Y.L., Yin, S.P., Yi, L.S., Fei, H.C., and Yang, Z.M., 2006, The Himalayan collision zone carbonatites in western Sichuan, SW China: Petrogenesis, mantle source and tectonic implication: Earth and Planetary Science Letters, v. 244, p. 234–250.
Hou, Z.Q., Tian, S.H., Xie, Y.L., Yang, Z.S., Yuan, Z.X., Yin, S.P., Yi, L.S., Fei, H.C., Zou, T.R., Bai, G., and Li, X.Y., 2009, The Himalayan Mianning-Dechang REE belt associated with carbonatite-alkaline complexes, eastern Indo-Asian collision zone, SW China: Ore Geology Reviews, v. 36, p. 65–89.
Hou, Z.Q, Liu, Y., Tian, S.H., Yang, Z.M., and Xie, Y.L., 2015, Formation of carbonatite-related giant rare-earth-element deposits by the recycling of marine sediments: Scientific Reports, v. 5, no. 10231.
Ickert, R.B., Hiess, J., Williams, I.S., Holden, P., Ireland, T.R., Lanc, P., Schram, N., Foster, J.J., and Clement, S.W., 2008, Determining high precision, in situ, oxygen isotope ratios with a SHRIMP II: Analyses of MPI-DING silicate-glass reference materials and zircon from contrasting granites: Chemical Geology, v. 257, p. 114–128.
Kemp, A.I.S., Hawkesworth, C.J., Foster, G.L., Paterson, B.A., Woodhead, J.D., Hergt, J.M., Grey, C.M., and Whitehouse, M.J., 2007, Magmatic and crustal differentiation history of granitic rocks from Hf-O isotopes in zircon: Science, v. 315, p. 980–983.
Li, Q.L., 2016, "High-U effect" during SIMS zircon U-Pb dating: Bulletin of Mineralogy, Petrology and Geochemistry, v. 35, p. 405–412.
Li, X.C., and Zhou, M.F., 2015, Multiple stages of hydrothermal REE remobilization recorded in fluorapatite in the Paleoproterozoic Yinachang Fe-Cu-(REE) deposit, southwest China: Geochimica et Cosmochimica Acta, v. 166, p. 53–73.
——2018, The nature and origin of hydrothermal REE mineralization in the Sin Quyen deposit, northwestern Vietnam: Economic Geology, v. 113, p. 645–673.
Li, X.C., Zhou, M.F., Chen, W.T., Zhao, X.F., and Tran, M.D., 2018, Uranium-lead dating of hydrothermal zircon and monazite from the Sin Quyen Fe-Cu-REE-Au-(U) deposit, northwestern Vietnam: Mineralium Deposita, v. 53, p. 399–416.
Liang, J.L., Ding, X., Sun, X.M., Zhang, Z.M., Zhang, H., and Sun, W.D., 2009, Nb/Ta fractionation observed in eclogites from the Chinese Continental Scientific Drilling Project: Chemical Geology, v. 268, p. 27–40.
Lichtervelde, M.V., Melcher, F., and Wirth, R., 2009, Magmatic vs. hydrothermal origins for zircon associated with tantalum mineralization in the Tanco pegmatite, Manitoba, Canada: American Mineralogist, v. 94, p. 439–450.
Ling, X.-X., Li, Q.-L., Liu, Y., Yang, Y.-H., Liu, Y., Tang, G.Q., and Li, X.-H., 2016, In situ SIMS Th-Pb dating of bastnaesite: Constraint on the mineralization time of the Himalayan Mianning-Dechang rare earth element deposits: Journal of Analytical Atomic Spectrometry, v. 31, p. 1680–1687.
Liu, Y., and Hou, Z.Q., 2017, A synthesis of mineralization styles with an integrated genetic model of carbonatite-nordmarkite-hosted REE deposits in the Cenozoic Mianning-Dechang REE metallogenic belt, the eastern Tibetan Plateau, southwestern China: Journal of Asian Earth Science, v. 137, p. 35–79.
Liu, Y., Hu, Z., Gao, S., Günther, D., Xu, J., Gao, C., and Chen, H., 2008, In situ analysis of major and trace elements of anhydrous minerals by LA-ICP-MS without applying an internal standard: Chemical Geology, v. 257, p. 34–43.
Liu, Y., Hou, Z.Q., Tian, S.H., Zhang, Q.C., Zhu, Z.M., and Liu, J.H., 2015a, Zircon U-Pb ages of the Mianning-Dechang nordmarkites, Sichuan Province, southwestern China: Constraints on the giant REE mineralization belt and its regional geological setting: Ore Geology Reviews, v. 64, p. 554–568.
Liu, Y., Zhang, R.Q., Zhang, Z.Y., Shi, G.H., Zhang, Q.C., Abuduwayiti, M., and Liu, J.H., 2015b, Mineral inclusions and SHRIMP U-Pb dating of zircons from the Alamas nephrite and granodiorite: Implications for the genesis of a magnesian skarn deposit: Lithos, v. 212–215, p. 128–144.
Liu, Y., Zhu, Z.M., Chen, C., Zhang, S.P., Sun, X., Yang, Z.S., and Liang, W., 2015c, Geochemical and mineralogical characteristics of weathered ore in the Dalucao REE deposit, Mianning-Dechang REE belt, western Sichuan Province, southwestern China: Ore Geology Reviews, v. 71, p. 437–456.
Liu, Y., Zhang, R.Q., Abuduwayiti, M., Wang, C., Zhang, S.P., Shen, C.H., Zhang, Z.Y., He, M.Y., Zhang, Y., and Yang, X.D., 2016, SHRIMP U-Pb zircon ages, mineral compositions and geochemistry of placer nephrite in the Yurungkash and Karakash River deposits, West Kunlun, Xinjiang, northwest China: Implication for a magnesium skarn: Ore Geology Reviews, v. 72, p. 699–727.
Liu, Y., Chakhmouradian, A.R., Hou, Z.Q., Song, W.L., and Kynicky, J., 2019, Development of REE mineralization in the giant Maoniuping deposit (Sichuan, China): Insights from mineralogy, fluid inclusions, and trace-element geochemistry: Mineralium Deposita, v. 54, p. 701–718.
Ludwig, K.R., 2001, Squid 1.02: A user's manual: Berkeley, California, Berkeley Geochronology Center, p. 15–35.
——2003, Mathematical-statistical treatment of data and errors for ^{230}Th/U geochronology: Uranium series: Geochemistry, v. 16, p. 631–656.
Lv, Y.J., Loucks, R.R., Fiorentini, M., McCuaig, T.C., Evans, N., Yang, Z.M., Hou, Z.Q., Kirkland, C., Parra-Avila, L.A., and Kobussen, A., 2016, Zircon compositions as a pathfinder for porphyry Cu ± Mo ± Au deposits: Society of Economic Geologists, Special Publication 19, p. 329–347.
Marsellos, A.E., and Garver, J.I., 2010, Radiation damage and uranium concentration in zircon as assessed by Raman spectroscopy and neutron irradiation: American Mineralogist, v. 95, p. 1192–1201.
Middlemost, E.A.K., 1994, Naming materials in the magma/igneous rock system: Earth Science Reviews, v. 37, p. 215–224.
Muñoz, M., Charrier, R., Fanning, C.M., Maksaev, V., and Deckart, K., 2012, Zircon trace element and O-Hf isotope analyses of mineralized intrusions from El Teniente ore deposit, Chilean Andes: Constraints on the source and magmatic evolution of porphyry Cu-Mo related magmas: Journal of Petrology, v. 53, p. 1091–1122.
Murakami, T., Chakoumakos, B.C., Ewing, R.C., Lumpkin, G.R., and Weber, W.J., 1991, Alpha-decay event damage in zircon: American Mineralogist, v. 76, p. 1510–1532.
Nasdala, L., Wenzel, M., Vavra, G., Irmer, G., Wenzel, T., and Kober, B., 2001, Metamictisation of natural zircon: Accumulation versus thermal annealing of radioactivity-induced damage: Contributions to Mineralogy and Petrology, v. 141, p. 125–144.
Nasdala, L., Reiners, P.W., Garver, J.I., Kennedy, A.K., Stern, R.A., Balan, E., and Wirth, R., 2004, Incomplete retention of radiation damage in zircon from Sri Lanka: American Mineralogist, v. 89, p. 219–231.
Nasdala, L., Miletich, R., Ruschel, K., and Váczi, T., 2008, Raman study of radiation-damaged zircon under hydrostatic compression: Physics and Chemistry of Minerals, v. 35, p. 597–602.
Palenik, C.S., Nasdala, L., and Ewing, R.C., 2003, Radiation damage in zircon: American Mineralogist, v. 88, p. 770–781.
Pearce, J.A., and Cann, J.R., 1973, Tectonic setting of basic volcanic rocks determined using trace-element analyses: Earth and Planetary Science Letters, v. 19, p. 290–300.
Pearce, N.J.G., Perkins, W.T., Westgate, J.A., Gorton, M.P., Jackson, S.E., Neal, C.R., and Chenery, S.P., 1997, A compilation of new and published major and trace element data for NIST SRM610 and NIST SRM612 glass reference materials: Geostandards Newsletter, v. 21, p. 115–144.
Peccerillo, A., and Taylor, S.R., 1976, Geochemistry of Eocene calc-alkaline volcanic rocks from the Kastamonu area, northern Turkey: Contributions to Mineralogy and Petrology, v. 58, p. 63–81.
Pettke, T., Audetat, A., Schaltegger, U., and Heinrich, C.A., 2005, Magmatic-hydrothermal crystallization in the W-Sn mineralized mole granite (NSW, Australia)—part II: Evolving zircon and thorite trace element chemistry: Chemical Geology, v. 220, p. 191–213.
Pupin, J.P., 1980, Zircon and granite petrology: Contributions to Mineralogy and Petrology, v. 73, p. 207–220.
Putnis, A., and Austrheim, H., 2010, Fluid-induced processes: Metasomatism and metamorphism: Geofluids, v. 10, p. 254–269.
Putnis, C.V., Tsukamoto, K., and Nishimura, Y., 2015, Direct observation of pseudomorphism: Compositional and textural evolution at a fluid-solid interface: American Mineralogist, v. 90, p. 1909–1912.
Rubin, J.N., Henry, C.D., and Price, J.G., 1989, Hydrothermal zircons and zircon overgrowths, Sierra Blanca Peaks, Texas: American Mineralogist, v. 74, p. 865–869.
——1993, The mobility of zirconium and other immobile elements during hydrothermal alteration: Chemical Geology, v. 110, p. 29–47.
Shu, X.C., and Liu, Y., 2019, Fluid inclusion constraints on the hydrothermal evolution of the Dalucao carbonatite-related REE deposit, Sichuan Province, China: Ore Geology Reviews, v. 107, p. 41–57.
Song, W.L., Xu, C., Smith, M.P., Chakhmouradian, A., Brenna, M., Kynicky, J., Chen, W., Yang, Y.H., Deng, M., and Tang, H.Y., 2018, Genesis of the world's largest rare earth element deposit, Bayan Obo, China: Protracted mineralization evolution over ~1 b.y.: Geology, v. 46, p. 323–326.
Standardization Administration of China, 2010, Methods for chemical analysis of silicate rocks—part 30: Determination of 44 elements: China National Standard GB/T 14506.1–2010 (in Chinese).

Stern, R.A., and Amelin, Y., 2003, Assessment of errors in SIMS zircon U-Pb geochronology using a natural zircon standard and NIST SRM 610 glass: Chemical Geology, v. 197, p. 111–142.
Takehara, M., Horie, K., Hokada, T., and Kiyokawa, S., 2018, New insight into disturbance of U-Pb and trace-element systems in hydrothermally altered zircon via SHRIMP analyses of zircon from the Duluth gabbro: Chemical Geology, v. 484, p. 168–178.
Tian, S.H., Hou, Z.Q., Su, A., Qiu, L., Mo, X.X., Hou, K.J., Zhao, Y., Hu, W.J., and Yang, Z.S., 2015, The anomalous lithium isotope signature of Himalayan collisional zone carbonatites in western Sichuan, SW China: Enriched mantle source and petrogenesis: Geochimica et Cosmochimica Acta, v. 159, p. 42–60.
Tu, X.L., Zhang, H., Deng, W.F., Ling, M.X., Liang, H.Y., Liu, Y., and Sun, W.D., 2011, Application of resolution in-situ laser ablation ICP-MS in trace element analyses: Geochimica, v. 40, p. 83–98 (in Chinese with English abs.).
Veksler, I.V., Dorfman, A.M., Kamenetsky, M., Dulski, P., and Dingwell, D.B., 2005, Partitioning of lanthanides and Y between immiscible silicate and fluoride melts, fluorite and cryolite and the origin of the lanthanide tetrad effect in igneous rocks: Geochimica et Cosmochimica Acta, v. 69, p. 2847–2860.
Wang, C.M., Bagas, L., Lv, Y.J., Santosh, M., Du, B., and McCuaig, T.C., 2016, Terran boundary and spatio-temporal distribution of ore deposits in the Sanjiang Tethyan orogen: Insights from zircon Hf-isotopic mapping: Earth Science Reviews, v. 156, p. 36–59.
Wang, C.M., Deng, J., Bagas, L., and Wang, Q., 2017, Zircon Hf-isotopic mapping for understanding crustal architecture and metallogenesis in the Eastern Qinling orogen: Gondwana Research, v. 50, p. 293–310.
Wang, X.L., Zhou, J.C., Wan, Y.S., Kitajima, K., Wang, D., Bonamici, C., Qiu, J.S., and Sun, T., 2013, Magmatic evolution and crustal recycling for Neoproterozoic strongly peraluminous granitoids from southern China: Hf and O isotopes in zircon: Earth and Planetary Science Letters, v. 366, p. 71–82.
Wang, X.L., Coble, M.A., Valley, J.W., Shu, X.J., Kitajima, K., Spicuzza, M.J., and Sun, T., 2014, Influence of radiation damage on Late Jurassic zircons from southern China: Evidence from in situ measurements of oxygen isotopes, laser Raman, U-Pb ages, and trace elements: Chemical Geology, v. 389, p. 122–136.
Woolley, A.R., and Kjarsgaard, B.A., 2008, Carbonatite occurrences of the world: Map and database: Geological Survey of Canada, Open-File Report 5796, p. 6–12.
Yang, W.B., Niu, H.C., Shan, Q., Sun, W.D., Zhang, H., Li, N.B., Yang, Y.H., and Yu, X.Y., 2014, Geochemistry of magmatic and hydrothermal zircon from the highly evolved Baerzhe alkaline granite: Implications for Zr-REE-Nb mineralization: Mineralium Deposita, v. 49, p. 451–470.
Yang, Y.H., Wu, F.Y., Li, Y., Yang, J.H., Xie, L.W., Liu, Y., Zhang, Y.B., and Huang, C., 2014, U-Pb dating of bastnaesite by LA-ICP-MS: Journal of Analytical Atomic Spectrometry, v. 29, p. 1017–1023.
Yuan, Z.X., Shi, Z.M., Bai, G., Wu, C.Y., Chi, R.A., and Li, X.Y., 1995, The Maoniuping rare earth ore deposit, Mianning County, Sichuan Province: Beijing, Seismological Publishing House, 150 p. (in Chinese).
Zeng, L.J., Niu, H.C., Bao, Z.W., and Yang, W.B., 2017, Chemical lattice expansion of natural zircon during the magmatic-hydrothermal evolution of A-type granite: American Mineralogist, v. 102, p. 655–665.
Zhao, W.W., Zhou, M.F, and Chen, W.T., 2016, Growth of hydrothermal baddeleyite and zircon in different stages of skarnization: American Mineralogist, v. 101, p. 2689–2700.
Zheng, X., and Liu, Y., 2019, Mechanisms of element precipitation in carbonatite-related rare-earth element deposits: Evidence from fluid inclusions in the Maoniuping deposit, Sichuan Province, southwestern China: Ore Geology Reviews, v. 107, p. 218–238.

Yan Liu received his B.Sc. degree from China University of Geosciences (Beijing) in 2002. He obtained a Ph.D. degree in 2010, also from China University of Geosciences (Beijing). Then he joined the Institute of Geology, Chinese Academy of Geological Sciences, as a postdoctoral researcher under the supervision of Hou Zengqian. From 2010 until now, his study has focused on REE mineralization, transportation, and precipitation during magmatic-hydrothermal processes in the Dalucao, Maoniuping, Lizhuang, and Muluzhai deposits and REE formation era and tectonic background along the Mianning-Dechang belt, Sichuan Provinces, and other carbonatite-related REE deposits in China.